

MAGNETO-ACOUSTIC WAVES IN SUNSPOTS: FIRST RESULTS FROM A NEW 3D NONLINEAR MAGNETOHYDRODYNAMIC CODE

T. FELIPE^{1,2}, E. KHOMENKO^{1,2,3} AND M. COLLADOS^{1,2}

Draft version March 24, 2022

ABSTRACT

Waves observed in the photosphere and chromosphere of sunspots show complex dynamics and spatial patterns. The interpretation of high-resolution sunspot wave observations requires modeling of three-dimensional non-linear wave propagation and mode transformation in the sunspot upper layers in realistic spot model atmospheres. Here we present the first results of such modeling. We have developed a 3D non-linear numerical code specially designed to calculate the response of magnetic structures in equilibrium to an arbitrary perturbation. The code solves the 3D nonlinear MHD equations for perturbations; it is stabilized by hyper-diffusivity terms and is fully parallelized. The robustness of the code is demonstrated by a number of standard tests. We analyze several simulations of a sunspot perturbed by pulses of different periods at subphotospheric level, from short periods, introduced for academic purposes, to longer and realistic periods of three and five minutes. We present a detailed description of the three-dimensional mode transformation in a non-trivial sunspot-like magnetic field configuration, including the conversion between fast and slow magneto-acoustic waves and the Alfvén wave, by calculation of the wave energy fluxes. Our main findings are the following: (1) the conversion from acoustic to the Alfvén mode is only observed if the the driving pulse is located out of the sunspot axis, but this conversion is energetically inefficient; (2) as a consequence of the cut-off effects and refraction of the fast magneto-acoustic mode, the energy of the evanescent waves with periods around 5 minutes remains almost completely below the level $\beta = 1$; (3) waves with frequencies above the cut-off propagate field-aligned to the chromosphere and their power becomes dominating over that of evanescent 5-minute oscillations, in agreement with observations.

Subject headings: MHD; Sun: chromosphere; Sun: oscillations; Sun: photosphere; sunspots

1. INTRODUCTION

Sunspots can be considered as laboratories for studies of magnetized plasma in conditions that are inaccessible on Earth. They give clues about the physics of energy propagation (*e.g.*, in the form of different oscillatory modes) in fluids permeated by strong magnetic fields. From the analysis of wave propagation it is possible to infer basic properties of stellar atmospheres. Waves observed in active regions are believed to have a relevant role in the energy balance of the solar atmosphere, being one of the candidates to explain the chromospheric heating. The first detection of waves in sunspots was done by Beckers & Tallant (1969), who called them “umbral flashes”. Since this date waves have been found in many solar features, from photospheric flux tubes to the solar wind.

Oscillations show a different behavior in different regions of sunspots. In the umbral photosphere their power spectrum peaks around 3 mHz (period of 5 minutes), and their amplitudes are around a hundred m s^{-1} . Waves in the photosphere of sunspot umbrae are similar to those observed in the quiet sun, but with their power reduced by a factor of 2–5 (Woods & Cram 1981). Several mechanisms have been proposed to explain this power suppression: reduction of wave excitation inside

sunspots (Goldreich & Keeley 1977; Goldreich & Kumar 1988, 1990), p -mode absorption inside sunspots (Cally 1995), different heights of spectral line formation due to the Wilson depression and altering of p -mode eigenfunctions by the magnetic field (Hindman et al. 1997).

Chromospheric umbral oscillations have a major power peak around 5 mHz (period of 3 minutes) and amplitudes of several kilometers per second. Velocities measured in chromospheric umbrae show saw-tooth temporal profiles, typical for shock waves (Lites 1986; Centeno et al. 2006). To explain the multiple peaks in the 3 minute band in the power spectrum of the chromospheric waves several hypotheses have been investigated: a resonant chromospheric cavity (Zhugzhda et al. 1985); non-linear interaction of photospheric modes (Gurman & Leibacher 1984); slow magneto-acoustic mode field-aligned propagation from the photosphere to the chromosphere in the 5–6 mHz band (Centeno et al. 2006).

In the penumbra the dominant oscillatory phenomena are running penumbral waves, which are best seen in H α core velocity observations as disturbances propagating radially outward from the umbra. As they move across the penumbra their radial velocity is apparently reduced and their frequencies also decrease from 4–5 mHz near the umbral/penumbral boundary to around 0.7–1.5 mHz at the outer edge of the penumbra (Bogdan & Judge 2006).

It is now becoming apparent that the photospheric 5-minute oscillations, chromospheric 3-minute oscillations, and running penumbral waves are the different manifestation of the same global dynamical phenomenon

tobias@iac.es

¹ Instituto de Astrofísica de Canarias, 38205, C/ Vía Láctea, s/n, La Laguna, Tenerife, Spain

² Departamento de Astrofísica, Universidad de La Laguna, 38205, La Laguna, Tenerife, Spain

³ Main Astronomical Observatory, NAS, 03680, Kyiv, Ukraine

(van der Voort et al. 2003; Bloomfield et al. 2007). No fully comprehensive model of this global oscillation phenomenon was presented up to date due to the complicated mathematical description of the physical processes playing a role in realistic magneto-atmospheres. The recent progress in observations and numerical simulations of sunspot waves is summarized in Khomenko (2010).

Although a lot of analytical work was done in simple atmospheres (Ferraro & Plumpton 1958; Zhugzhda & Dzhililov 1984, to name a few), those works were restricted to very idealized cases. Numerical simulations allow more flexibility and over the last years many attempts were done to perform numerical modelling of waves in non-trivial magnetic field configurations, with applications to the photosphere and the chromosphere (*e.g.* Cargill et al. 1997; Rosenthal et al. 2002; Hasan et al. 2003; Bogdan et al. 2003; Hasan & Ulmschneider 2004; Hasan et al. 2005; Khomenko & Collados 2006; Khomenko et al. 2008). In most of the cases, these works were restricted to studies of the behavior of high-frequency waves (above cut-off) in two-dimensional situations. Despite these limitations, several important questions were learned from these models. It was shown that the fast magneto-acoustic mode in the magnetically dominated region (*i.e.* where the sound speed c_S is much lower than the Alfvén speed v_A) is refracted and reflected down to the gas pressure dominated atmosphere due to the gradients of the Alfvén speed (Khomenko & Collados 2006). Earlier, Rosenthal et al. (2002) demonstrated that the inclination of the magnetic field lines is important for the fast mode reflection, *i.e.* in those regions where the inclination angle is large almost all of the fast mode wave energy is reflected back down. Another important feature of all these simulations is the presence of the mode transformation at the layer where $v_A = c_S$. Around this layer, the phase speeds of all modes are similar and different waves can interact (Bogdan et al. 2003; Cally 2006; Khomenko & Collados 2006). The direction and efficiency of the mode transformation depends on the frequency of the wave and the angle between the wave vector and the magnetic field (Cally 2005, 2006). When this angle is small and the frequency is high, the fast mode can be converted into the slow mode and vice versa.

Most of the works cited above on the simulations of wave propagation in the upper layers of sunspots, as well as the analytical theories of the mode transformation, were developed for high-frequency waves with frequencies above, or just at, the cut-off frequency. There is another class of simulations where the problem of helioseismic wave propagation below sunspots is addressed and waves with realistic solar frequencies in the 3-5 mHz range are considered (Cally & Bogdan 1997; Parchevsky & Kosovichev 2009; Hanasoge 2008; Cameron et al. 2008; Moradi et al. 2009b; Khomenko et al. 2009). In the latter works most attention has been paid to the wave propagation in subsurface layers, rather than in upper photospheric and chromospheric layers. Thus, there is gap between these two kind of models. With the development of our code and its first results presented here we pretend to cover this gap and to address the problem of three dimensional propagation and transformation of the 3-5 mHz period waves in the upper layers of sunspots. Our aim is to

investigate the response of the magnetic atmospheres to oscillations with low frequencies (like 5-minute waves) and to compare this response with that from the high-frequency perturbations. As those 5-minute waves have most power at the photospheric heights and are used in measurements to derive the parameters of the solar atmosphere, including solar active regions, understanding their propagation and transformation properties is important. Our objective is to perform numerical calculations sufficiently realistic to imitate the wave excitation in sunspots, reproduce the change of wave frequency with height, formation of shocks at chromospheric layers, and to be at the level allowing comparison with photospheric and chromospheric observations by spectral synthesis.

Several numerical codes have been developed among the solar physics community to study the propagation of waves in magnetized atmospheres. They adopt different strategies for the numerical scheme, boundary conditions and wave driving, having their advantages and disadvantages (Moradi et al. 2009a). The upper boundary typically represents a problem in wave simulations, since waves should not artificially be reflected there back into the physical domain. Rosenthal et al. (2002) apply characteristic boundary conditions at the top boundary; Hasan et al. (2005) uses the open boundary concept; while Khomenko et al. (2008) introduced a special media at the top called Perfectly Matched Layer (PML) which absorbs with almost no reflections the waves that reach the upper boundary. Rosenthal et al. (2002) and Hasan et al. (2005) solve the complete MHD equations, while Khomenko et al. (2008) solve equations for perturbations with all non-linear terms retained. This strategy gives them an advantage for precision of the numerical scheme and for the application of the boundary conditions.

3D MHD codes for wave simulations are starting to be available. Cameron et al. (2007) presented the semi-spectral linear MHD code SLiM, developed for helioseismology purposes. In this code, the horizontal derivatives are evaluated in Fourier space and the upper boundary is treated as a sponge layer. Another 3D linear MHD code for wave propagation has been developed by Parchevsky & Kosovichev (2007). The authors use the realistic OPAL equation of state and a PML layer as the upper boundary condition. Numerically, the upper magnetized atmospheric layers represent an additional problem limiting strongly the time step of the simulations due to the high values of the Alfvén speed. To overcome this problem, one of the strategies used is the Lorentz force controller. This method consists in reducing the amplitude of the Lorentz force in the layers where the Alfvén speed is large. This method is used by Hanasoge (2008) in his 3D linear code. However, the influence of this artificial procedure on the simulated wave properties has not been verified yet. Recently Shelyag et al. (2008) presented a nonlinear 3D parallel code developed on the base of the VAC code (Tóth 1996). In this code, they use the same philosophy as Khomenko et al. (2008), solving non-linear equations for perturbations. As for sunspots, only results of the 2D helioseismic wave propagation below surface have been presented so far from this code (Shelyag et al. 2009), not addressing the wave propagation in the upper layers.

The non-linear MHD code described in this paper rep-

resents an extension of the code by Khomenko et al. (2008) into three dimensions. Our code solves the MHD equations for perturbations in a background plasma in magnetohydrostatic equilibrium using artificial diffusion to assure numerical stability of the solution, and is fully MPI-parallelized. In this paper we present extensive numerical tests demonstrating the code stability and robustness. We also present the first scientific results of the three-dimensional wave propagation and transformations in the upper atmosphere of a sunspot model. Our first aims are to study the propagation of waves, excited by sub-photospheric pulses, up to the chromosphere, including the shock wave formation. We present a detailed description of the three-dimensional mode transformation for waves with different frequencies, from below to above the acoustic cut-off frequency. In particular, we address the question of conversion to Alfvén waves in realistic conditions. Works on conversion from/to Alfvén waves in three dimensions are only now being initiated (*e.g.* Cally & Goossens 2008) and no generalized picture has been obtained yet. The organization of the paper is as follows. In Section 2 we describe the MHD equations and the numerical details of the calculations. In Section 3 we discuss the results of the simulations of the three-dimensional wave propagation and mode transformation in a sunspot model. This section includes the description of the magneto-static sunspot model in equilibrium (Section 3.1) and a brief discussion of the dispersion relations and wave propagation speeds (Section 3.2). Section 4 presents our conclusions and our future plans for the application of the code. Finally, in Appendix A, we show several numerical tests applied to prove the robustness of the code.

2. NUMERICAL PROCEDURE

2.1. MHD equations

Our numerical code is an extension to 3 dimensions of the code described in Khomenko & Collados (2006); Khomenko et al. (2008). It solves the non-linear equations of ideal compressible MHD. Written in conservative form, these equations are:

$$\frac{\partial \rho}{\partial t} + \nabla \cdot (\rho \mathbf{v}) = 0, \quad (1)$$

$$\frac{\partial(\rho \mathbf{v})}{\partial t} + \nabla \cdot \left[\rho \mathbf{v} \mathbf{v} + \left(p + \frac{\mathbf{B}^2}{2\mu_0} \right) \mathbf{I} - \frac{\mathbf{B}\mathbf{B}}{\mu_0} \right] = \rho \mathbf{g} + \mathbf{S}(t), \quad (2)$$

$$\frac{\partial e}{\partial t} + \nabla \cdot \left[\mathbf{v} \left(e + p + \frac{|\mathbf{B}|^2}{2\mu_0} \right) - \frac{1}{\mu_0} \mathbf{B}(\mathbf{v} \cdot \mathbf{B}) \right] = \rho(\mathbf{g} \cdot \mathbf{v}) + Q_{\text{rad}}, \quad (3)$$

$$\frac{\partial \mathbf{B}}{\partial t} = \nabla \times (\mathbf{v} \times \mathbf{B}), \quad (4)$$

where \mathbf{I} is the identity tensor, ρ is the density, \mathbf{v} is the velocity, p is the gas pressure, \mathbf{B} is the magnetic field, \mathbf{g} is the gravitational acceleration and e is the total energy per unit volume,

$$e = \frac{1}{2} \rho v^2 + \frac{p}{\gamma - 1} + \frac{B^2}{2\mu_0}. \quad (5)$$

The dot ‘.’ represents the scalar product of vectors, while the notation ‘ $\mathbf{B}\mathbf{B}$ ’ stands for the tensor product. The energy losses Q_{rad} can be described by the Newton

law of cooling, but, in the simulations presented in this paper, it is set to zero. We neglect the viscous force, the thermal conduction and the terms describing the diffusion of the magnetic field. However, artificial equivalents of some of these terms are introduced later for the issue of numerical stability of the simulations. The term $\mathbf{S}(t)$ in Eq. 2 represents a time-dependent external force.

In an equilibrium state, where temporal derivatives and velocities are null, and in the absence of external forces ($\mathbf{S} = 0$), the previous equations reduce to the equations of the force balance for a gravitationally stratified magnetized plasma:

$$\nabla \cdot \left[\left(p_0 + \frac{\mathbf{B}_0^2}{2\mu_0} \right) \mathbf{I} - \frac{\mathbf{B}_0 \mathbf{B}_0}{\mu_0} \right] = \rho_0 \mathbf{g}. \quad (6)$$

Considering departures from the equilibrium state induced by an external force \mathbf{S} , ρ , p and \mathbf{B} can be expressed as the sum of the background value (subindex 0) and the perturbation (subindex 1):

$$\rho = \rho_0 + \rho_1, \quad (7)$$

$$p = p_0 + p_1, \quad (8)$$

and

$$\mathbf{B} = \mathbf{B}_0 + \mathbf{B}_1, \quad (9)$$

while the velocity only corresponds to a perturbed value $\mathbf{v} = \mathbf{v}_1$.

The non-linear equations for perturbations are obtained by replacing expressions (7–9) in Eqs. (1–4) and subtracting the equation of the magnetohydrostatic equilibrium (Eq. 6). The following system of MHD equations for perturbations of density, pressure, magnetic field and velocities is obtained in conservative form:

$$\frac{\partial \rho_1}{\partial t} + \nabla \cdot [(\rho_0 + \rho_1) \mathbf{v}_1] = 0, \quad (10)$$

$$\begin{aligned} & \frac{\partial [(\rho_0 + \rho_1) \mathbf{v}_1]}{\partial t} + \nabla \cdot \left[(\rho_0 + \rho_1) \mathbf{v}_1 \mathbf{v}_1 + \left(p_1 + \frac{\mathbf{B}_1^2}{2\mu_0} + \frac{\mathbf{B}_1 \mathbf{B}_0}{\mu_0} \right) \mathbf{I} - \frac{1}{\mu_0} (\mathbf{B}_0 \mathbf{B}_1 - \mathbf{B}_1 \mathbf{B}_0 - \mathbf{B}_1 \mathbf{B}_1) \right] = \\ & = \rho_1 \mathbf{g} + \left(\frac{\partial [(\rho_0 + \rho_1) \mathbf{v}_1]}{\partial t} \right)_{\text{diff}} + \mathbf{S}(t), \end{aligned} \quad (11)$$

$$\begin{aligned} & \frac{\partial e_1}{\partial t} + \nabla \cdot \left[\mathbf{v}_1 \left((e_0 + e_1) + (p_0 + p_1) + \frac{|\mathbf{B}_0 + \mathbf{B}_1|^2}{2\mu_0} \right) - \frac{1}{\mu_0} (\mathbf{B}_0 + \mathbf{B}_1) (\mathbf{v}_1 \cdot (\mathbf{B}_0 + \mathbf{B}_1)) \right] = \\ & = (\rho_0 + \rho_1) (\mathbf{g} \cdot \mathbf{v}_1) + Q_{\text{rad}} + \left(\frac{\partial e_1}{\partial t} \right)_{\text{diff}}, \end{aligned} \quad (12)$$

$$\frac{\partial \mathbf{B}_1}{\partial t} = \nabla \times [\mathbf{v}_1 \times (\mathbf{B}_0 + \mathbf{B}_1)] + \left(\frac{\partial \mathbf{B}_1}{\partial t} \right)_{\text{diff}}, \quad (13)$$

Artificial diffusion terms have been added to Eqs. (11–13) compared to Eqs. (2–4). The diffusivity terms in Eqs. (11–13) have their physical counterparts and are

needed for reasons of stability of the simulations. A similar strategy is applied in the MURAM code (Vögler et al. 2005).

The code solves the above system of non-linear equations for perturbations. The use of equations for perturbations instead of the complete equations for wave simulations has two big advantages. Firstly, the terms describing the static model and those for perturbations can vary by orders of magnitude. Thus, by excluding equilibrium terms we avoid important numerical precision problems. Secondly, the boundary conditions are easier to implement on equations for perturbations (see § 2.5).

In high layers, where the magnetic pressure is much larger than the gas pressure, Eq. (12) is numerically problematic as recovering thermal energy (p) from total energy (e) leads to numerical errors. In these layers it is replaced by the equation describing the balance of the internal energy

$$\frac{\partial p_1}{\partial t} + \mathbf{v}_1 \nabla (p_0 + p_1) + c_S^2 \left[\nabla \left((\rho_0 + \rho_1) \mathbf{v}_1 \right) - \mathbf{v}_1 \nabla (\rho_0 + \rho_1) \right] = (\gamma - 1) \rho_1 Q_{\text{rad}} + \left(\frac{\partial p_1}{\partial t} \right)_{\text{diff}}. \quad (14)$$

The transition from one equation to the other is done smoothly using the plasma parameter β as a criterion.

The gravity \mathbf{g} is constant with height and the equation of state of an ideal gas with constant γ is used to link the thermal variables.

The computational domain is discretized using a three-dimensional Cartesian grid with constant space step in each dimension. The spatial derivatives are approximated by a centered, fourth order accurate, explicit finite differences scheme using five grid points (Vögler et al. 2005). The solution is advanced in time by an explicit fourth-order Runge-Kutta. The fourth order differences allow to give an accurate solution, still resolving shock fronts, which is difficult with higher-order methods.

2.2. Artificial diffusivity

To damp high-frequency numerical noise on sub grid scales, we replace the physical diffusive terms in the equations of momentum and energy by artificial equivalents. In the induction equation we retain the magnetic diffusion term, replacing η by an artificial value. In general, we use a philosophy similar to Stein & Nordlund (1998), Caunt & Korpi (2001) and Vögler et al. (2005). Each physical quantity has its own diffusivity coefficient (scalar/vectorial for scalar/vectorial quantities), which is formed by a shock resolving term, a hyperdiffusivity part and a constant contribution:

$$\nu_l(u) = \nu_l^{\text{shk}}(u) + \nu_l^{\text{hyp}}(u) + \nu_l^0, \quad (15)$$

where $\nu_l^0 = (c_S + v_A) \Delta x_l F(x, y, z)$, u is the corresponding quantity, $F(x, y, z)$ gives the form of the constant contribution and $\Delta x_l \equiv \Delta x, \Delta y, \Delta z$.

2.3. Time step

The time step has to ensure that the physical dependence domain is included inside the numerical dependence domain. According to this, the mesh width must be bigger than the distance traveled by the information in a single time step due to mass flow, waves or diffusion transport. The time step must be chosen to be smaller than the advective time step and the time step imposed by the diffusion terms:

$$\Delta t \leq \min(\Delta t_v, \Delta t_{\text{diff}}) \quad (16)$$

In this expression Δt_v is the time step imposed by a modified CFL condition, approximately valid for MHD equations,

$$\Delta t_v = \left[\frac{c_v}{1/\Delta x^2 + 1/\Delta y^2 + 1/\Delta z^2} \right]^{1/2} \frac{1}{v_{\text{max}}} \quad (17)$$

where v_{max} is the maximum value of the sound and Alfvén speeds. The time step imposed by the diffusion Δt_{diff} corresponds to the minimum of the diffusion time across the three dimensions,

$$\Delta t_{\text{diff}} = c_{\text{diff}} \min \left(\frac{\Delta x^2}{\nu_x}, \frac{\Delta y^2}{\nu_y}, \frac{\Delta z^2}{\nu_z} \right) \quad (18)$$

where the constant coefficients c_v and c_{diff} are taken to be below one to ensure the stability of the solution. The diffusion coefficients $\nu_{x,y,z}$ are those defined in § 2.2.

2.4. Filtering

In the particular case of wave simulations high diffusion is not desirable since it modifies the wave amplitudes. At the same time, low diffusion can not always prevent the developing of high frequency noise. In such cases we perform an additional filtering of small wavelengths. Following Parchevsky & Kosovichev (2007) we use a sixth-order digital filter to eliminate unresolved short-wave components:

$$u_{\text{filt}} = u(x) - \sum_{m=-3}^3 d_m u(x + m\Delta x), \quad (19)$$

where u is a variable before filtering and u_{filt} is after filtering. The filter can be applied in the three spatial coordinates independently. The coefficients d_m have been chosen to construct the filtering function:

$$G(k\Delta x) = 1 - \sum_{m=-3}^3 d_m e^{imk\Delta x} = 1 - \sin^6 \left(\frac{k\Delta x}{2} \right). \quad (20)$$

The frequency of application of the filter depends on the simulation, but it is usually applied every 10 seconds.

2.5. Boundary conditions

Boundary conditions are an important issue for wave simulations. One usually wants to prevent spurious wave reflections at the boundaries. Two strategies commonly applied are based on characteristic boundary conditions or sponge layer. Calculating characteristic conditions (Rosenthal et al. 2002), apart from tricky, gives good results in simple magnetic field configurations, when the

wave propagation directions are easily predictable. For more complex magnetic field configurations, the calculation of the characteristic directions is not an easy task. The other alternative, *i.e.*, sponge layer, consists in locating an absorbing layer at the boundary to dissipate the wave energy and prevent it from coming back to the physical domain. This strategy is implemented in the code SLiM (Cameron et al. 2007). Absorbing layers give goods results only when the absorption is gradual and needs a large amount of grid points. Thus, numerically they are very costly. In our code we used yet another alternative, the Perfectly Matched Layer (Berenger 1994).

The Perfect Matched Layer (PML) is designed to absorb waves without reflections. This method was first introduced by Berenger (1994) to absorb electromagnetic waves in numerical solutions of Maxwell equations. Later it has been applied to Euler equations (Hu 1996) and to simulations of acoustic waves in a strongly stratified solar convection zone (Parchevsky & Kosovichev 2007). In our code we extend the method to the full set of the MHD equations (Eqs. 10–13). The MHD equations can be written schematically, in conservative form, as:

$$\frac{\partial \mathbf{u}}{\partial t} + \frac{\partial \mathbf{F}(\mathbf{u})}{\partial x} + \frac{\partial \mathbf{G}(\mathbf{u})}{\partial y} + \frac{\partial \mathbf{K}(\mathbf{u})}{\partial z} = \mathbf{H}(\mathbf{u}), \quad (21)$$

where $\mathbf{u} \equiv [\rho_1, (\rho_0 + \rho_1)\mathbf{v}_1, e_1, \mathbf{B}_1]$ is the vector that contains the conserved variables; the vectors \mathbf{F} , \mathbf{G} and \mathbf{K} are the fluxes, whose expressions can be found in the system (10–13); and \mathbf{H} represents the source terms at right-hand side of the same equations. Inside the PML, variables \mathbf{u} are split into three components in such a way that $\mathbf{u} = \mathbf{u}_1 + \mathbf{u}_2 + \mathbf{u}_3$ and also $\mathbf{H}(\mathbf{u}) = \mathbf{H}_1(\mathbf{u}) + \mathbf{H}_2(\mathbf{u}) + \mathbf{H}_3(\mathbf{u})$ and the system of MHD equations is split into a set of three coupled, one dimensional equations:

$$\frac{\partial \mathbf{u}_1}{\partial t} + \frac{\partial \mathbf{F}(\mathbf{u})}{\partial x} + \sigma_x(x)\mathbf{u}_1 = \mathbf{H}_1(\mathbf{u}), \quad (22)$$

$$\frac{\partial \mathbf{u}_2}{\partial t} + \frac{\partial \mathbf{G}(\mathbf{u})}{\partial y} + \sigma_y(y)\mathbf{u}_2 = \mathbf{H}_2(\mathbf{u}), \quad (23)$$

$$\frac{\partial \mathbf{u}_3}{\partial t} + \frac{\partial \mathbf{K}(\mathbf{u})}{\partial z} + \sigma_z(z)\mathbf{u}_3 = \mathbf{H}_3(\mathbf{u}). \quad (24)$$

These split Eqs. (22–24) are solved independently in the PML, in contrast to the unsplit forms (Eq. 21) which are solved in the physical domain.

An absorption term has been added to each equation. The coefficients $\sigma_x(x)/\sigma_y(y)/\sigma_z(z)$ only depend on x/y/z coordinate and are non-zero in the x/y/z PML faces, respectively. Theoretically, a PML with constant absorption coefficient produces no reflections for plane waves incident on a flat interface for any angle of incidence and any frequency. However, due to the finite difference implementation of the PML equations in numerical calculations, reflections may appear when σ has a steep gradient (Berenger 1996). To solve this problem it is necessary to include smooth variations in the absorption coefficients from small values at the interface between the PML medium and the physical domain to large values at the outer boundary. Following Hu (2001), good results are obtained with absorption coefficients of the form:

$$\sigma_x = \frac{a}{\Delta x} \left(\frac{x - x_{\text{PML}}}{x_{\text{PML}}} \right)^2 \quad (25)$$

$$\sigma_y = \frac{b}{\Delta y} \left(\frac{y - y_{\text{PML}}}{y_{\text{PML}}} \right)^2 \quad (26)$$

$$\sigma_z = \frac{c}{\Delta z} \left(\frac{z - z_{\text{PML}}}{z_{\text{PML}}} \right)^2 \quad (27)$$

where Δx , Δy and Δz are the discretization steps, a , b and c are constants controlling the damping amplitude, and x_{PML} , y_{PML} and z_{PML} are the thickness of the PML domain in each spatial direction. In a typical calculation we need a PML with 10–15 grid points. The coefficients a , b and c depend on each particular simulation and are proportional to the wave speed at the boundaries. We locate PMLs at all boundaries of our simulation domain. The results presented in Khomeiko et al. (2008) show that this strategy gives good results even for strong shocks.

The PML formulation, as presented above, can become unstable in long simulation runs. According to the literature (see, *e.g.*, Hesthaven 1998), a high frequency noise filtering can improve the long-time stability of the PML layer. We found that this method works well for MHD waves. Applying a filter allows to delay the effects of the possible instability the necessary time to complete long enough simulation runs. Previously the PML layer for MHD wave simulations was applied by Parchevsky & Kosovichev (2009), though the stability of the PML formulation for MHD equations was not discussed in this paper.

The code can also account for periodic and closed boundary conditions.

2.6. Parallelization

Parallelization has been done with MPI following a distributed memory concept in which all data used by a processor are situated on the memory partition accessible to it. Data are split in a certain number of processors by means of a domain decomposition scheme. The full numerical domain is divided into a set of three dimensional subdomains, with communication between processors only occurring at their common data boundaries. For this purpose, each domain includes three layers of “ghost” cells at each boundary. The 5-point stencil of the fourth-order scheme needs two cells outside the subdomain, while for the filtering it is necessary to include one more “ghost” layer. The boundaries of the subdomains which are neighbors of other subdomains receive directly the required information and store it in the “ghost” layers, while when the boundary of the subdomain coincides with the global boundary, the “ghost” layers are settled with the values imposed by the boundary condition.

We have performed a number of standard numerical tests, as well as tests specifically devised for wave propagation, to prove the robustness of the numerical method and of the boundary conditions. The results of these tests are given in Appendix A.

3. 3D PROPAGATION AND TRANSFORMATION OF WAVES IN SUNSPOT MODEL

Below in this Section we discuss several simulations of the propagation and transformation of MHD waves in a

magnetostatic sunspot model, excited by pulses with different periods and locations. To facilitate the reading of this section, Table 1 summarizes the simulation runs. It gives the number of the sub-section where the results are presented, the properties of the driver, its location, horizontal source size, the duration of the simulations and the numbers of the corresponding figures. In all cases, to identify the different wave modes in three spatial dimensions we use projections of the velocity into three characteristic directions. To quantify the mode transformation we calculate the acoustic and magnetic energy fluxes (see Section 3.3).

We use a vertical force in the momentum equation $\mathbf{S}(t)$ to perturb a magnetostatic sunspot atmosphere in equilibrium and study the waves generated by this perturbation. We have performed several numerical simulations, all of them with the source situated below the quiet photosphere at $z = -0.5$ Mm and $y = 0$ Mm, but with differences in the period, the horizontal x location of the source relative to the axis of the sunspot, as well as the horizontal size of the source R_{src} .

In the simulations described in Sect. 3.4, 3.5 and 3.6 the temporal behavior of the driver is harmonic is described by the expression:

$$S_z(r, t) = AP(r) \sin \frac{2\pi t}{\tau} \quad (28)$$

In this equation, A is the amplitude of the source, $P(r) = [1 - (r/R_{\text{src}})^2]^2$ describes the source shape, R_{src} is the source radius, $r = \sqrt{(x - x_{\text{src}})^2 + (y - y_{\text{src}})^2 + (z - z_{\text{src}})^2}$ is the distance from the source center and τ is the period of the harmonic source. $P(r)$ is zero if $r > R_{\text{src}}$. The x and y components of \mathbf{S} , $S_x(r, t)$ and $S_y(r, t)$, are set to zero.

In the simulations described in Section 3.7 the behavior of the driver is not harmonic in time, but rather has a shape of Ricker wavelet:

$$S_z(r, t) = AP(r) (1 - 2\tau_0^2) e^{-\tau_0^2} \quad (29)$$

where $\tau_0 = \omega_0 t / 2 - \pi$. Such driver produces a spectrum of waves with a central frequency ω_0 (Parchevsky & Kosovichev 2009). We set $\omega_0 = 3.33$ mHz, so the spectrum of our driver resembles a solar one and covers a broad range of frequencies.

This latter run is particularly interesting, as it allows us to study the behavior of a realistic spectrum of solar waves in the upper layers (photosphere and chromosphere) of a sunspot model, including the propagation of individual wave modes and wave energy fluxes. As far as we are aware of, no such investigation has been performed as of today.

3.1. Magnetostatic sunspot model

Here we use a magnetostatic (MHS) model atmosphere in equilibrium representative of a sunspot, adopted from Khomenko & Collados (2008). This MHS model is a thick flux tube with distributed currents, it is azimuthally symmetric and has no twist. The variations of field strength and gas pressure are continuous across the spot. At 40 Mm far from the sunspot axis the model merges smoothly into a quiet Sun atmosphere taken from the model S (Christensen-Dalsgaard et al. 1996) in the

deep sub-photosphere layers and continuing as a VAL-C model (Vernazza et al. 1981) in the photospheric and chromospheric layers. The sunspot axis in the atmospheric layers is given by the semi-empirical model of Avrett (1981). The dimensions of our computational domain are 2.5 Mm in the vertical direction and 15 Mm in each horizontal direction with a grid size of $\Delta z = 25$ km and $\Delta x = \Delta y = 75$ km. The bottom level is 1.25 Mm below $\tau_{5000} = 1$ at the photospheric quiet sun atmosphere, which was chosen as the zero level of the coordinate z . The top level is 1.25 Mm above $z = 0$. A PML layer of 10 grid points was used at both bottom and top boundaries. With this, the physical domain occupies from $z = -1$ Mm to $z = 1$ Mm. The axis of the sunspot is placed at the center of the simulation domain. The magnetic field at the axis is about 900 G at $z = 0$ Mm.

3.2. Dispersion relations and propagation directions

In a three-dimensional situation like the one considered here, three types of wave modes exist: fast and slow magneto-acoustic waves and the Alfvén wave. Each of these modes is described by its own dispersion relation, *i.e.* relation between its temporal frequency and the wave number $\omega = \omega(\mathbf{k})$. The modes are characterized by their own phase velocity, $\mathbf{v}_{\text{ph}} = \omega/\mathbf{k}$, and the group velocity, $\mathbf{v}_{\text{g}} = \partial\omega/\partial\mathbf{k}$. The first one is parallel to the direction of \mathbf{k} and gives the wave front propagation velocity. The second one defines the direction of the energy propagation. The magnitudes and directions of \mathbf{v}_{ph} and \mathbf{v}_{g} usually do not coincide.

In a 3D homogeneous unstratified atmosphere permeated by a constant magnetic field \mathbf{B}_0 , parallel to z axis, and y axis normal the plane defined by the direction of propagation \mathbf{k} and \mathbf{B}_0 , the generalized wave equation for the perturbations decouples into two, defining the dispersion relation for the three MHD modes:

$$\frac{\omega}{k} = v_A \cos \varphi, \quad (30)$$

$$\frac{\omega^2}{k^2} = \frac{1}{2}(v_A^2 + c_S^2) \pm \frac{1}{2}\sqrt{(v_A^2 + c_S^2)^2 - 4v_A^2 c_S^2 \cos^2 \varphi}, \quad (31)$$

where $v_A = (B_0^2/\mu_0\rho_0)^{1/2}$ is the Alfvén speed, $c_S = (\gamma p_0/\rho_0)^{1/2}$ is the sound speed, and φ is the angle between \mathbf{k} and \mathbf{B}_0 .

Equation (30) describes an Alfvén wave, whose associated perturbations in \mathbf{v}_1 and \mathbf{B}_1 are transversal to \mathbf{B}_0 and \mathbf{k} and the perturbations in pressure and density are zero. For the propagation along the magnetic field the phase velocity of this wave is equal to v_A . The energy of the Alfvén mode propagates along magnetic field lines, according to its group velocity.

The solutions with the plus and minus sign in Eq. (31) are the fast and slow modes, respectively. When one of the c_S or v_A is much higher than the other, the dispersion equation (Eq. 31) can be simplified to $\omega = kv_{\text{fast}}$ for the fast mode and $\omega = kv_{\text{slow}} \cos \varphi = v_{\text{slow}} \mathbf{k} \cdot \mathbf{B}_0/|B_0|$ for the slow mode, where v_{fast} is the highest velocity between v_A and c_S and v_{slow} is the lowest. The direction of the phase and group velocities of the fast mode is \mathbf{k} and their magnitude is either c_S or v_A , so the energy propagates in the same direction as the wave front. The slow wave group velocity is directed along \mathbf{B}_0 . When c_S and v_A are similar, the behavior of the phase and group velocities of

TABLE 1
SUMMARY OF THE SIMULATION RUNS

Section	Driving	Location	R_{src}	Duration	Figures
4.4	50 s, harmonic	$x = 0$ Mm	150 km	904 s	7–12
4.5	50 s, harmonic	$x = -3$ Mm	150 km	1023 s	13–17
4.6	180 s, harmonic	$x = 0$ Mm	540 km	930 s	18
4.7	300 s, wavelet	$x = 0$ Mm	900 km	1511 s	19–21
4.7	300 s, harmonic	$x = 0$ Mm	900 km	1212 s	–

the fast and slow modes deviates from this simple picture, and can be retrieved from the derivation of \mathbf{v}_g from Eq. (31).

3.3. Identification of the wave modes in simulations

In the case of a real atmosphere, the division into pure wave modes is not so simple as in the idealized case described above, as often no clear distinction between the modes can be done neither physically nor mathematically. Even in the above simple case the governing partial differential equation factors into a single second order wave equation for the Alfvén mode and a fourth order wave equation for the coupled fast-slow modes, so the idea that there are three distinct modes may not always be correct. However, the simplicity of this picture makes it attractive and we will discuss the properties of the waves in realistic atmospheres in terms of the three modes.

To help the identification of the wave modes in simulations, we use the mode properties described above. We project the vectorial quantities (velocity and magnetic field perturbations) into the directions aligned/normal to the equilibrium magnetic field \mathbf{B}_0 .

At each location of the computational domain, we calculated the projections of the \mathbf{v}_1 and \mathbf{B}_1 into the following Cartesian directions:

$$\hat{e}_{\text{long}} = [\cos \phi \sin \theta, \sin \phi \sin \theta, \cos \theta], \quad (32)$$

$$\hat{e}_{\text{perp}} = [-\cos \phi \sin^2 \theta \sin \phi, 1 - \sin^2 \theta \sin^2 \phi, -\cos \theta \sin \theta \sin \phi], \quad (33)$$

$$\hat{e}_{\text{trans}} = [-\cos \theta, 0, \cos \phi \sin \theta]. \quad (34)$$

where θ is the magnetic field inclination from the vertical and ϕ is the field azimuth, measured from the $x - z$ plane. The direction of \hat{e}_{long} is along the magnetic field \mathbf{B}_0 . The direction of \hat{e}_{perp} is normal to the field and was chosen following Cally & Goossens (2008) as the asymptotic polarization direction of the Alfvén mode in the low- β regime. The last component $\hat{e}_{\text{trans}} = \hat{e}_{\text{long}} \times \hat{e}_{\text{perp}}$ is set in the direction normal to the other two.

We expect that in a region where $c_S > v_A$, the slow magneto-acoustic mode will be identified in \hat{e}_{trans} projection of the velocity vector, while the fast magneto-acoustic mode will be equally visible in all velocity components as it propagates isotropically. In a region where $c_S < v_A$, the slow magneto-acoustic mode will be identified projected into \hat{e}_{long} direction, the Alfvén mode projected into the \hat{e}_{perp} direction, and the fast magneto-acoustic mode in the the direction normal to these two.

To quantify the amount of energy contained in different wave modes and to develop a measure of the mode transformation, suitable in the case of complex magnetic field configurations like the one considered here, we found it useful to calculate the wave energy fluxes (Bray & Loughhead 1974). The acoustic energy flux is given by the expression:

$$\mathbf{F}_{\text{ac}} = p_1 \mathbf{v}_1, \quad (35)$$

and magnetic energy flux is given by:

$$\mathbf{F}_{\text{mag}} = \mathbf{B}_1 \times (\mathbf{v}_1 \times \mathbf{B}_0) / \mu_0. \quad (36)$$

The acoustic energy flux contains the energy of the wave with acoustic nature, which corresponds to the fast mode in the region where $v_A < c_S$, and to the slow mode in the region where $v_A > c_S$. In this region, the magnetic flux includes the fast and the Alfvén modes. Since, as we will see in the next section, in the region above the layer where $v_A = c_S$ the fast mode is refracted down towards the photosphere, the magnetic energy which propagates upwards along field lines must correspond to the Alfvén wave, making possible the identification of this mode.

3.4. Case of 50 s harmonic force located at the axis

Figure 1 presents a two-dimensional snapshot of some variables and Figure 2 gives the temporal evolution of the projected velocities in the simulation run with the harmonic 50 sec force located at the sunspot axis. The panels (a–c) in Figs. 1 show the longitudinal, transversal and perpendicular velocities scaled with a factor $\sqrt{\rho_0}$. These magnitudes provide the square root of the kinetic energy associated to the waves. Due to the strong density fall off, some velocity perturbations at high layers have so low energy that makes them indistinguishable in this representation. To make them visible, we have plotted additional contours of constant velocity. In the case of the pressure (Fig. 1e), its drop with height makes the absolute value of the perturbations at the lower layers much higher than at the upper layers. In this case, the contours represent the ratio of constant p_1/p_0 .

3.4.1. Propagation below the surface

The vertical force acts in a region where $c_S^2/v_A^2 \approx 9.1$ and it generates mainly an acoustic fast mode, whose oscillations can be seen in the longitudinal velocity, pressure and density snapshots in Fig. 1. This vertical impulse produces initially a deficit in density and pressure at the place where the source is located and, because of that, horizontal motions also appear, creating a magnetic slow mode seen in the transversal velocity and magnetic field snapshots in Fig. 1.

At photospheric level, the longitudinal velocity has an amplitude of about 200 m s^{-1} , the amplitude of transversal velocity is 50 m s^{-1} and the transversal magnetic field

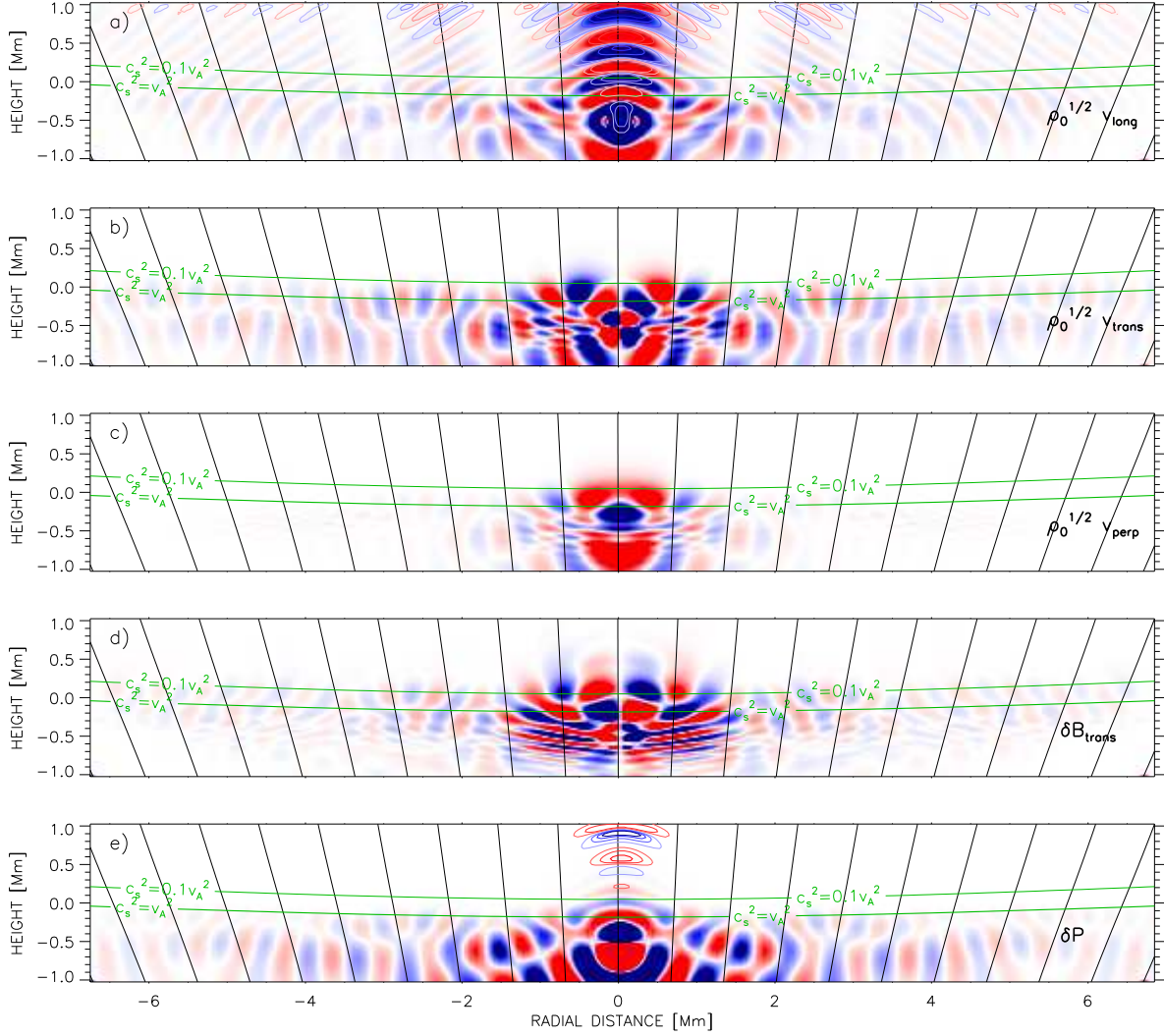


FIG. 1.— Variations of the velocity in the direction \hat{e}_{long} (a), \hat{e}_{trans} (b), and \hat{e}_{perp} (c), all of them scaled with factor $\sqrt{\rho_0}$ of the unperturbed density; magnetic field in the direction \hat{e}_{trans} (d), and pressure (e) at an elapsed time $t = 820$ s after the beginning of the simulations for the 50 s harmonic force located at $x = 0$ km, $y = 0$ km and $z = -500$ km. All panels show the plane $y = 0$ km, except panel (c), which shows $y = 400$ km. Black inclined lines are magnetic field lines. Green lines are contours of constant v_A^2/c_S^2 . The image color coding is such that blue colors represent lower values and red colors are higher values with respect to the mean. Scaling in panels (a), (b), (c) is the same. Figure (a) shows contours of equal longitudinal velocity, and (d) shows contours of equal p_1/p_0 .

oscillates with a maximum deviation from the equilibrium value of 4 G.

The temporal evolution given in Fig. 2 shows the fast mode (acoustic in nature) propagating in the deep layers upwards to the region where $v_A \approx c_S$. It appears as a perturbation in the longitudinal velocity (panels c–d). Variations in longitudinal velocity are accompanied by acoustic variations of pressure and density (not shown in the figure). The slow mode (of magnetic nature) is visible in the transverse the acoustic perturbation reaches the surface $v_A^2 = c_S^2$ earlier than the magnetic perturbation. In these deep layers, the acoustic oscillations have a wavelength larger than the magnetic ones. As the fast (acoustic) wave propagates in the region $v_A < c_S$, its energy is distributed in the three spatial dimensions and it decreases away from the source as $1/r^2$. Once it reaches the $v_A > c_S$ region, the energy redistribution in horizontal directions is not so important because it is channeled along the field lines and is only affected by the density

falloff.

3.4.2. Three-dimensional mode transformation

When the waves reach the $v_A^2 = c_S^2$ layer from below, several mode transformations take place in the simulation.

First of all, the fast acoustic mode moves from a region where $v_A < c_S$ to another where $v_A > c_S$ keeping its acoustic nature but changing from fast to slow mode. This transformation can be seen in the snapshots of longitudinal velocity and relative pressure in Fig. 1 (panels a and e) as the wavefronts above the layer $v_A^2 = c_S^2$. The atmosphere above $v_A^2 = c_S^2$ is dominated by the magnetic field and this slow acoustic mode propagates upwards along field lines (Fig. 2, a–c). The amplitude of this wave increases according to the density drop and it develops into shocks above $z = 500$ km. Figure 3 shows that the oscillations in the vertical velocity develop a clear saw-tooth shape with sudden decreases of the ve-

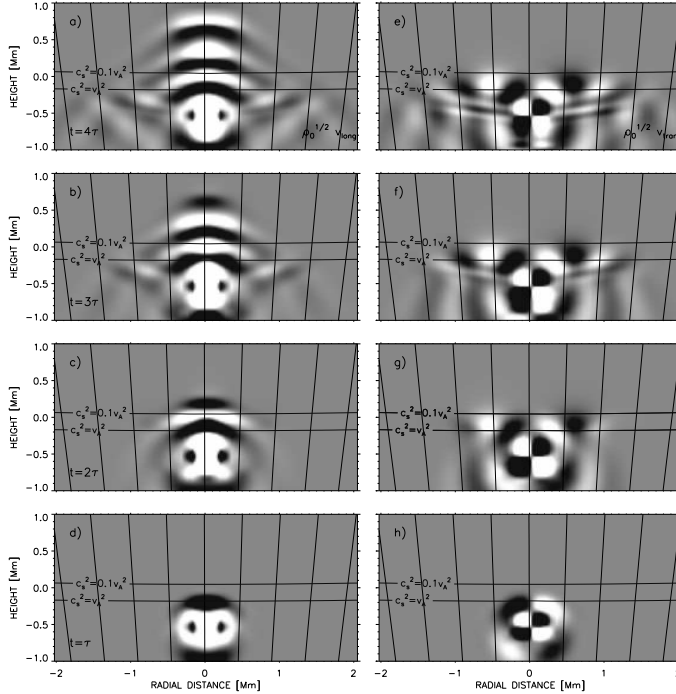


FIG. 2.— Time evolution of $\sqrt{\rho_0}v_{\text{long}}$ (left) and $\sqrt{\rho_0}v_{\text{trans}}$ (right) for the simulation with 50 s harmonic driver. Time increases from bottom to top, with an elapsed time between panels of a period (τ). The image color coding is such that black represents negative values and white represents positive values. Horizontal lines are contours of constant v_A^2/c_S^2 .

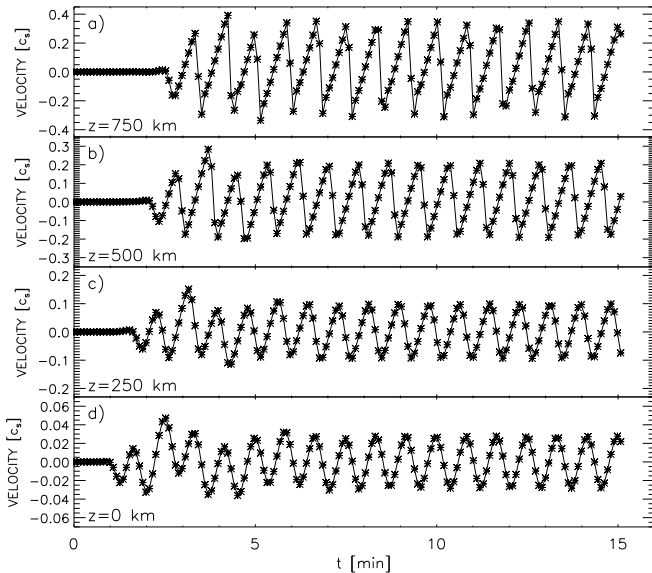


FIG. 3.— Vertical velocity in the units of local sound speed at the axis of the sunspot at several heights in the simulations with 50 s harmonic force. From bottom to top: $z = 0$ km, $z = 250$ km, $z = 500$ km and $z = 750$ km.

locity followed by slower increases. They present peak-to-peak variations of almost 8 km s^{-1} and their period is 50 s, the same period imposed by the excitation pulse.

The second mode transformation is the acoustic fast mode which is transmitted as a magnetic fast mode in the region $v_A > c_S$, where the magnetic field dominates.

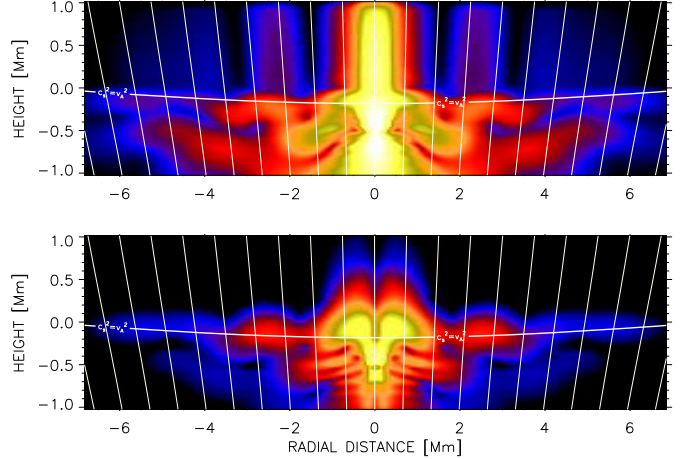


FIG. 4.— Acoustic (top) and magnetic (bottom) flux for the simulation with a 50 s harmonic driver located at the axis of the sunspot averaged over the stationary stage of the simulations. Horizontal white line is the height where sound speed and Alfvén speed are equal. Vertical lines are magnetic field lines. The axis are not to scale.

The evolution of this magnetic mode in the first 200 s of the simulation is clearly seen in Fig. 2 (panels e–g) in the transversal velocity as the wave which moves away from the axis of the sunspot just above the surface $v_A^2 = c_S^2$. This mode is also visible in the transversal magnetic field variations (Fig. 1d). Due to the rapid increase of the v_A with height the fast magnetic mode refracts and reflects back to the sub-photosphere, showing a behavior similar to the two-dimensional case considered by Khomenko & Collados (2006).

When the reflected magnetic fast wave reaches again the $v_A^2 = c_S^2$ layer, it suffers two new transformations: a fast to slow transformation, resulting in a magnetic wave in the $v_A < c_S$ region; and a fast to fast transmission, which produces a new acoustic wave below $v_A = c_S$. First, we discuss the slow magnetic wave. In Fig. 1 (panels b–d) it is clearly visible in the transversal and perpendicular velocities and the magnetic field variations, at horizontal locations inside a radius of 1.5 Mm around the axis and at heights between $z = -1$ Mm and $z = 0$ Mm. Observing the temporal evolution at the beginning of the simulation one can see that in Fig. 2g the fast magnetic wave above $v_A^2 = c_S^2$ has been refracted down and it is located between the two horizontal lines which indicate surfaces of constant v_A^2/c_S^2 , but it has not arrived to the lower one, so the new transformation has not been produced. In the next time step (Fig. 2f) the wave has already been transformed in a slow magnetic mode in the region below $v_A^2 = c_S^2$. The wavelength of this slow mode decreases as the wave propagates to deeper layers because of the drop of the Alfvén speed, which falls from 15 km s^{-1} at $z = 0$ Mm to 2 km s^{-1} at $z = -1$ Mm. Due to the higher density at the deeper layers the amplitude of this wave also decreases as it propagates down.

On the other hand, after the downward fast to fast transmission has occurred from the refracted fast wave, another fast acoustic wave appears in the region $v_A < c_S$. It is visible in longitudinal velocity Fig. 1a and in pressure in Fig. 1d below the layer $v_A^2 = c_S^2$. The presence of this new acoustic mode can be checked comparing Fig. 2c and Fig. 2b. In the latter one, there is a new wave

situated at both sides of the axis of the sunspot at a radial distance between 0.5 and 1.5 Mm which can be seen in longitudinal velocity. This mode appears after the reflected fast mode in the region $v_A > c_S$ reaches the surface $v_A^2 = c_S^2$. It propagates faster than the slow magnetic wave mentioned before, with a speed close to the sound speed, and its wavelength is larger than that of the slow mode. It keeps the direction of the incidence of the fast magnetic wave in the layer where $v_A^2 = c_S^2$, so it propagates down with some inclination with respect to the vertical, moving away from the axis.

In order to investigate the presence of the Alfvén mode in this simulation (either before or after the transformations) we have plotted in Fig. 1c the velocity component in the direction \hat{e}_{perp} . As expected, this velocity component has a node in the plane $y = 0$ Mm. Thus, we present in Fig. 1c a vertical cut out of this plane, at 0.4 Mm from the center of the computational domain. In this projection, the Alfvén wave, if present, should appear as velocity oscillation above $v_A^2 = c_S^2$ layer. The inspection of Fig. 1c shows that there are no oscillations in the magnetically dominated layers that can be identified as an Alfvén mode. Our conclusion is that when the wave driving occurs at the axis of the sunspot, no conversion to Alfvén waves happens.

3.4.3. Propagation in the upper atmosphere

Velocity contours in Fig. 1a show the presence of some waves at a radial distance between ± 1.5 and ± 6 Mm near the top of the computational domain. These waves are specially tricky. From the first look at the figures and from the time evolution of the snapshots one may have an impression (from the inclination of the wave front) that they propagate across field lines, opposite to the normal behavior of a slow acoustic wave. However, we verified that their propagation speed is equal to c_S , indicating their acoustic nature. The analysis of their wave numbers indicates that the direction of propagation of these waves is close to the inclination of the magnetic field lines. Thus, we came to the conclusion that these waves are slow acoustic waves created from the continuous transformation of the fast acoustic mode which moves away from the driver across the field lines below $v_A^2 = c_S^2$ (visible in Fig. 1b in transversal velocity and in Fig. 1d in pressure variations from a radial distance of ± 2 Mm to ± 6 Mm) when it reaches this layer. As the wave front closer to the axis of the sunspot gets to the surface $v_A^2 = c_S^2$ earlier, the slow acoustic wave that it produces has the wave front inclined in the direction to the axis. Due to this fact, it looks like its propagation is across the field lines. This hypothesis also explains the nodes located at a radial distance of ± 1.5 and ± 3 Mm.

3.4.4. Acoustic and magnetic wave energy fluxes

Figure 4 shows the acoustic and magnetic fluxes averaged over the stationary stage of the simulations. Around 95% of the flux at the location of the driver is acoustic flux and it corresponds to the fast mode. At the center of the sunspot, where the magnetic field is almost vertical, the fast to slow transformation is very effective and the region above the layer $v_A^2 = c_S^2$ at the axis is dominated by the slow acoustic mode. When the angle between the direction of propagation of the wave and the magnetic field is different from zero, the fast to fast transmission

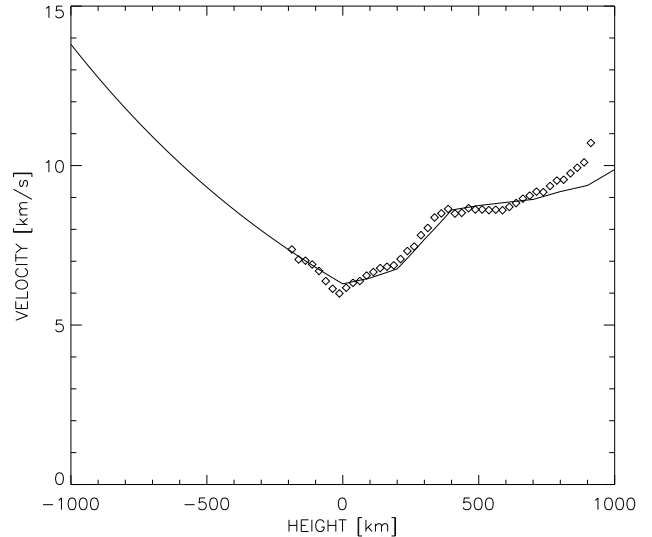


FIG. 5.— Sound speed profile (solid line) at the axis of the sunspot. Diamonds represent the phase velocity of the slow acoustic mode measured from the simulations with 50 s harmonic force.

is produced and it forms the two lobes which are visible in the magnetic flux just above the layer $v_A^2 = c_S^2$. The magnetic flux reaches a height of 0.5 Mm before the fast waves are refracted back toward the photosphere. In the low- β region, the fast magnetic mode has an important contribution from $z = 0$ Mm to $z = 0.5$ Mm for radial distances below 2 Mm, except at the axis of the sunspot. The transformation of the refracted fast magnetic wave when it comes back towards the photosphere generates acoustic as well as magnetic flux in the high- β region, corresponding to the new fast and slow modes, respectively, which propagate downwards. As expected, we do not find any propagating magnetic flux along the field lines, that may be associated with an Alfvén mode.

3.4.5. Slow acoustic mode phase velocities

The phase velocity of a linear high-frequency slow mode wave in a magnetically dominated region is equal to c_S . In our simulation, a slow acoustic wave appears above the $v_A^2 = c_S^2$ layer produced after the mode transformation. This wave allows us to check whether or not the velocity of waves involved in the simulations in this complex sunspot model corresponds to that expected from theoretical considerations.

Figure 5 presents the results of this test. The solid line in Figure 5 shows the stratification of the sound speed with height at the sunspot axis and diamonds indicate the phase velocity of the slow mode wave measured at each grid point from the simulations. Note that diamonds are only plotted at heights above $z = -200$ km, after the mode transformation has been completed. The velocity of the slow wave matches well the local sound speed at heights from $z = -200$ km to $z = 700$ km. Higher than $z = 700$ km the wave starts to propagate faster than c_S , since the velocity amplitude of the wave approaches the sound speed and non-linearities start playing an important role.

3.4.6. Slow acoustic mode amplitudes

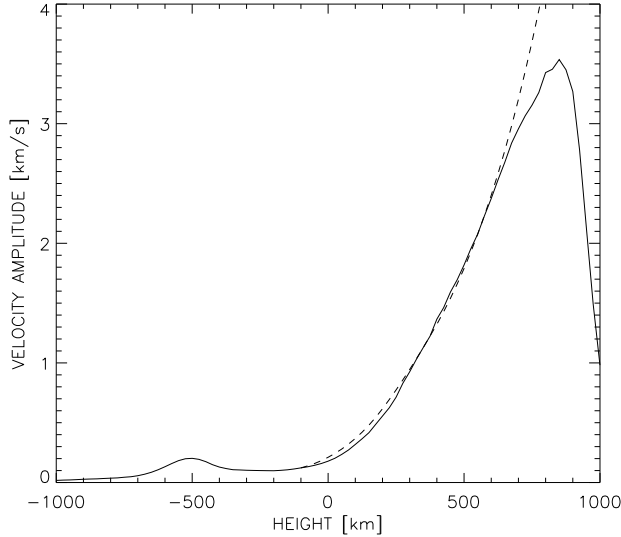


FIG. 6.— Amplitude of the slow acoustic mode vertical velocity (solid line) in the simulations with 50 s harmonic force. Dashed lines gives the analytical curve for an acoustic-gravity wave with 50 s period (Mihalas & Mihalas 1984).

As the slow acoustic wave propagates up in the atmosphere of the sunspot the amplitude of the velocity oscillations increases due to the density drop. The kinetic energy of this wave is proportional to ρv^2 and must be conserved. Thus, a decrease of the density must be accompanied with an increase of the velocity. The atmosphere of the sunspot is very complex and it includes vertical and horizontal gradients in all the magnitudes. Because of that there is no analytical expression for the variation of the amplitudes of the waves with height. However, we can compare the particular case of the wavefront of the slow acoustic mode wave which propagates along the axis of the sunspot with a case of a linear acoustic wave which propagates upwards in a gravitationally stratified atmosphere permeated by a magnetic field parallel to the direction of gravity. In this theoretical case, the amplitude of the wave is given by

$$A(z) = A_0 \exp\left(\int_{z_0}^z \frac{dz}{2H_0}\right), \quad (37)$$

In Fig. 6 we show the amplitude of the vertical velocity at each grid point at the axis of the sunspot (solid line) for the stationary stage of the simulations. The force is located at $z = -500$ km and the amplitude of the wave decreases until it reaches $z = -200$ km. This initial decrease is due to the part of the energy of the source that goes into other wave types because of the mode transformations. More or less at this layer the wave is transformed into a slow acoustic mode as it propagates up while its amplitude increases. When the wave reaches the height $z = 850$ km its amplitude drops very fast as a consequence of the large diffusivity that was imposed at high layers in order to stabilize the numerical simulation. In this figure is also overplotted the expected amplitude according to Eq. (37) (dashed line), starting from the height where the wave has already been transformed into a slow acoustic mode in the region $v_A > c_S$.

From $z = -200$ km to $z = 700$ km the numerical amplitude agrees with the analytical one, while from $z = 700$ km to $z = 850$ km the numerical amplitude is lower than the analytical one. This happens because the wave develops into weak shocks and the linear approximation for the amplitude increase is no longer valid. Note that the amplitudes of the oscillations (Fig. 6) as well as the phase velocity (Fig. 5) show discrepancies with the linear theory at the same heights.

3.5. Case of 50 s harmonic force located off the axis

Fig. 7 gives a three-dimensional view of the vertical velocity in the simulation run with 50 s harmonic force located at $x = -3$ Mm off the sunspot axis. This figure clearly shows the asymmetry of the wave front with respect to the axis. In the lower part of the domain, the fast (acoustic) waves can be appreciated propagating in circles away from the source with a visibly lower amplitude toward the axis. In the upper part of the domain, slow (acoustic) waves are the dominating ones, propagating along the inclined magnetic field lines.

Fig. 8 presents the projected velocities in the three characteristic directions at the horizontal cut of the simulation domain taken at the middle photosphere at $z = 300$ km. Fig. 9 shows the snapshots of some variables in the vertical cut through the domain. Both figures correspond to the same time moment of the simulations at $t = 820$ s. These simulations have many features in common with the previously considered case of the driving force located at the sunspot axis. A set of fast (acoustic) and slow (magnetic) modes is generated below the layer $v_A^2 = c_S^2$, propagating upwards and suffering several transformation after reaching this height. Similar to the previous case, slow (acoustic) and fast (magnetic) modes are produced after the mode transformation in the magnetically dominated upper atmosphere. The conversion to slow and fast modes in the low- β region only presents slight changes in comparison with the simulation with the driver placed at the axis. One of these changes is the presence of an asymmetry with respect to the axis. For example, the transformation of the downward propagating refracted fast (magnetic) mode into the slow (magnetic) mode below the surface (Fig. 9, panels b–d) presents such asymmetry. Due to the particular combination of the field inclination and the direction of propagation of the refracted fast mode, this transformation is much more efficient on the right from the source in the direction toward the axis (locations between $x = -3$ and -1 Mm at $z \approx -0.5$ Mm).

The most important changes are present in the velocity component in the direction \hat{e}_{perp} (Fig. 8c). At height of $z = 300$ km, this component shows variations that do not correspond to the fast (magnetic) mode. The latter has been already reflected down. As demonstrated by the analysis of the magnetic energy flux below, the variations observed in the snapshot of \hat{e}_{perp} at heights above $z \approx 300$ km at locations between $x = -4 \div -2$ Mm and $y = -1 \div 1$ Mm correspond to the Alfvén wave.

The acoustic and magnetic fluxes are shown in Fig. 10. These fluxes, in general, show a pattern similar to the case of driving at the axis, but some important asymmetry is also present. The acoustic flux of the slow mode in the low- β region is oriented in the direction of the field lines and it is slightly lower than in the previous simu-

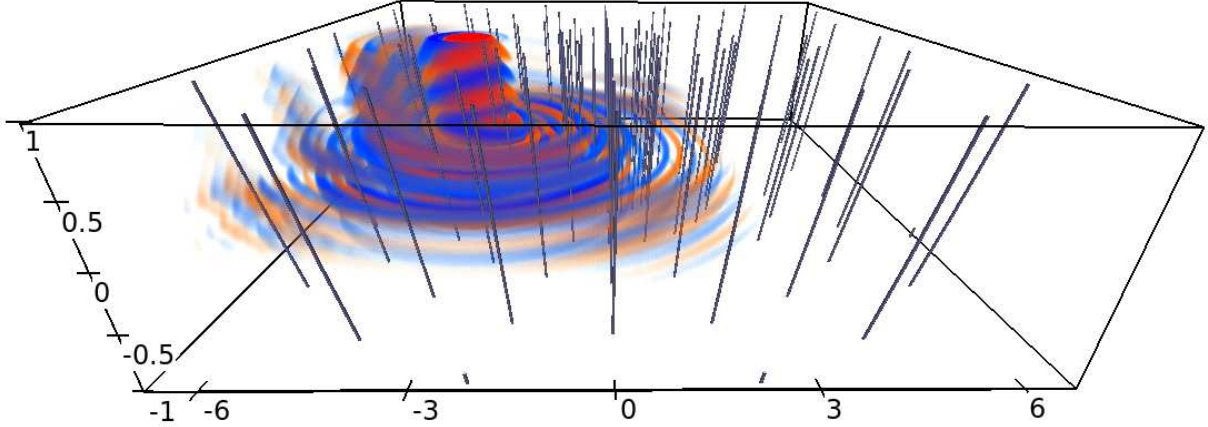


FIG. 7.— Variations of $\sqrt{\rho}v_z$ at an elapsed time $t=820$ s after the beginning of the simulations for the 50 s harmonic force at 3 Mm from the axis of the sunspot. Grey inclined lines are magnetic field lines. Blue colors represent upward movement while orange/red colors are downward movement.

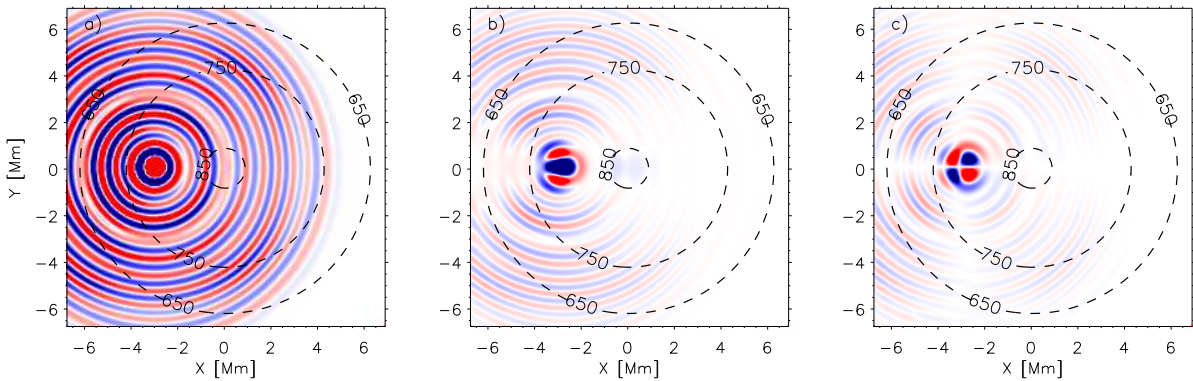


FIG. 8.— Variations of the velocity in the direction \hat{e}_{long} (a), \hat{e}_{trans} (b), and \hat{e}_{perp} (c), all of them scaled with factor $\sqrt{\rho_0}$ of the unperturbed density, at $z = 300$ km and at an elapsed time $t = 820$ s after the beginning of the simulations for the 50 s harmonic force located at $x = -3$ Mm, $y = 0$ Mm and $z = -0.5$ Mm. The image color coding is such that blue colors represent lower values and red colors are higher values with respect to the mean. All images have the same scale. Concentric dashed lines are contours of equal magnetic field.

lation due to the larger angle between the direction of propagation of the fast mode before reaching the layer $v_A^2 = c_S^2$ and the magnetic field (φ). An important fraction of the magnetic flux appears in the lobe located at $v_A^2 = c_S^2$ line in the direction toward the axis of the sunspot present due to more efficient fast to fast mode transmission with increasing φ (Cally 2005). Compared to Fig. 4 there is also more magnetic flux present in the upper part of the atmosphere above $v_A^2 = c_S^2$, apparently directed along the magnetic field lines. It is not clear, however, whether this flux corresponds to fast, not yet completely reflected wave, or to the Alfvén wave. To clarify this issue we have calculated the magnetic flux following Eq. (36), but using only velocity and magnetic field projections in the direction \hat{e}_{perp} . We expect that the longitudinal projection of this quantity gives us indications about the presence of the propagating Alfvén waves.

Figure 11 illustrates the result. Top panel corresponds to a vertical cut in the plane $y = -0.4$ Mm, normalized at every height to its maximum value at this height. The bottom panel is a horizontal cut in the plane $z = 0.9$ Mm. The white colors (positive flux) mean upward energy

propagation, while the black colors (negative flux) mean downward energy propagation. Indeed these plots reveal the energy flux associated to the Alfvén wave, which clearly propagates upwards along the field lines. The Alfvén mode has a node at the plane $y = 0$ Mm, where the driver was located, so conversion to this mode is only produced when the wave vector forms a certain angle with the magnetic field (different from zero). This result is in qualitative agreement with the recent investigation of the conversion to Alfvén waves by (Cally & Goossens 2008). However, even at the location where the contribution of the Alfvén wave energy flux to the total energy flux is maximum, its flux is still around 20 times lower than the acoustic flux at this location. So it means that in the sunspot magnetic field configuration and for the driver location considered here, the transformation from fast (acoustic) to Alfvén wave is much less effective than the transformation to the slow (acoustic) wave in the magnetically dominated upper atmosphere.

3.6. Case of 180 s harmonic force located at the axis

This simulation shows many features which also appeared in the 50 s harmonic case, since the response of

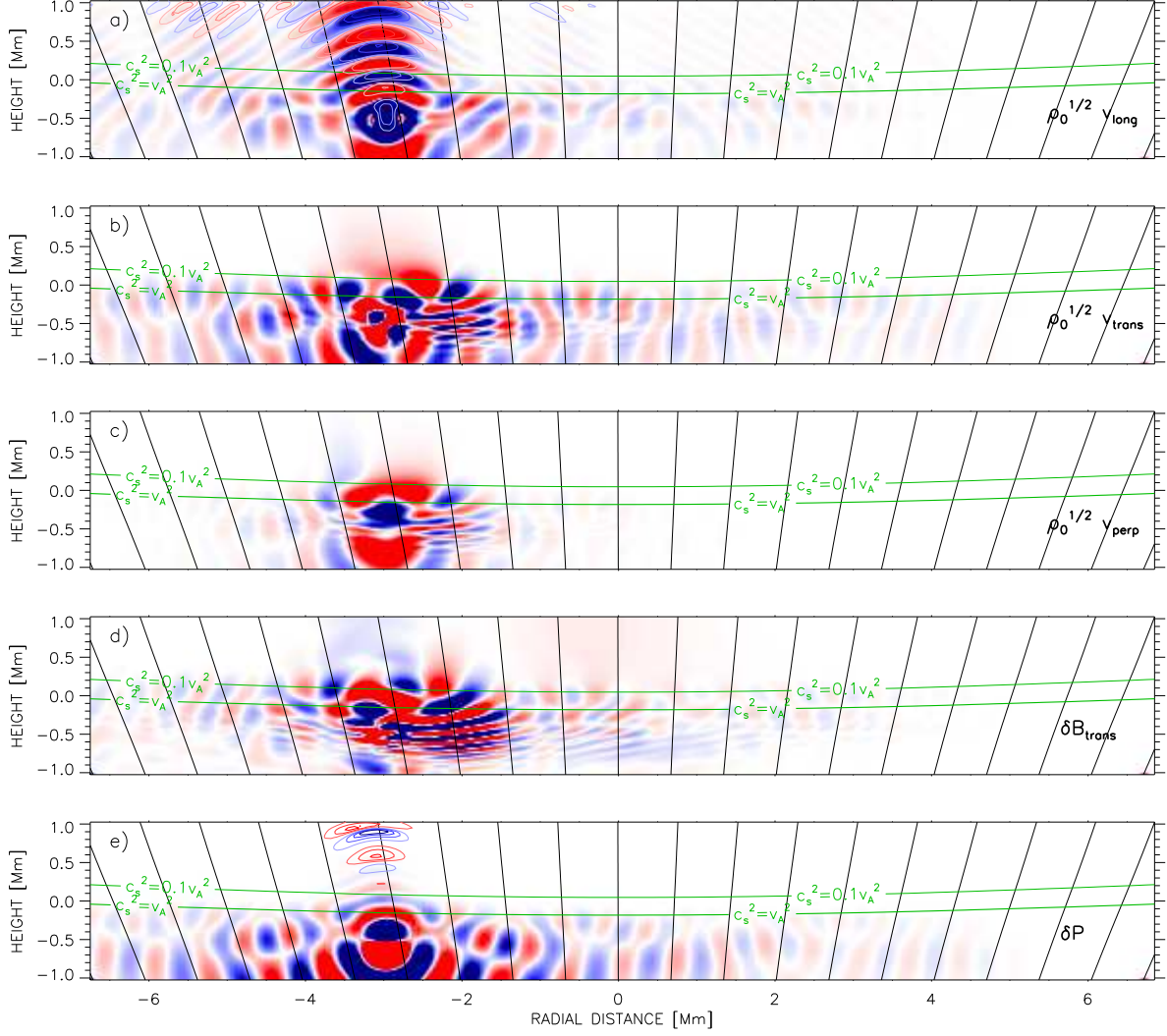


FIG. 9.— Variations of the velocity in the direction \hat{e}_{long} (a), \hat{e}_{trans} (b), and \hat{e}_{perp} (c), all of them scaled with factor $\sqrt{\rho_0}$ of the unperturbed density; magnetic field in the direction \hat{e}_{trans} , (d) and pressure (e) at an elapsed time $t=820$ s after the beginning of the simulations for the 50 s harmonic force located at $x = -3$ Mm off the sunspot axis. The format of the figure is the same as Fig. 1.

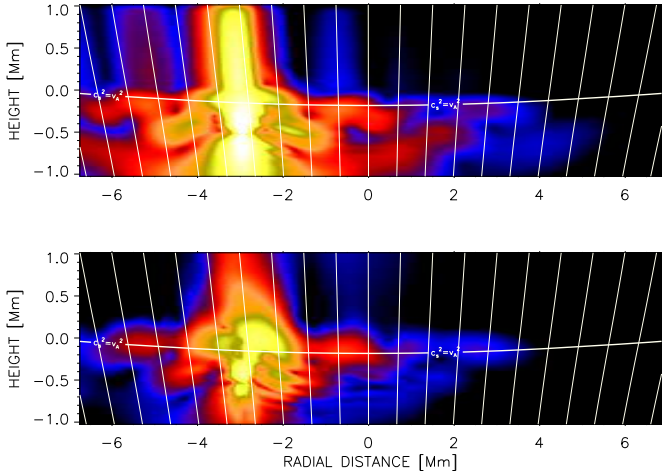


FIG. 10.— Average acoustic (*top*) and magnetic (*bottom*) flux for the 3D simulation with a 50 s harmonic driver located at 3 Mm from the axis of the sunspot averaged over the stationary stage of the simulations. The format is the same as Fig. 4.

the magnetic atmosphere is quite similar at both frequencies because they are above the cut-off frequency. So, in this case we omit the discussion of the mode transformation and only show results of the acoustic and magnetic flux calculations. These fluxes are presented in Fig. 12.

This figure is very similar to Fig. 4, except for much larger wavelength of the fluctuations, in agreement with the larger temporal period of waves. The average acoustic flux shows that at the axis of the sunspot the fast to slow mode transformation is also effective for waves with 180 s period. After the transformation, slow (acoustic) waves propagate acoustic energy upwards. The fast mode visible in the magnetic flux above the $v_A^2 = c_S^2$ also has longer wavelengths than in the 50 s harmonic simulation. The magnetic flux vanishes at the axis of the sunspot at high layers. Due to the reflection of the fast (magnetic) wave, there is no magnetic flux above the certain height, also away from the axis. In this simulation we find no traces of the Alfvén mode.

3.7. Case of 300 s wavelet force located at the axis

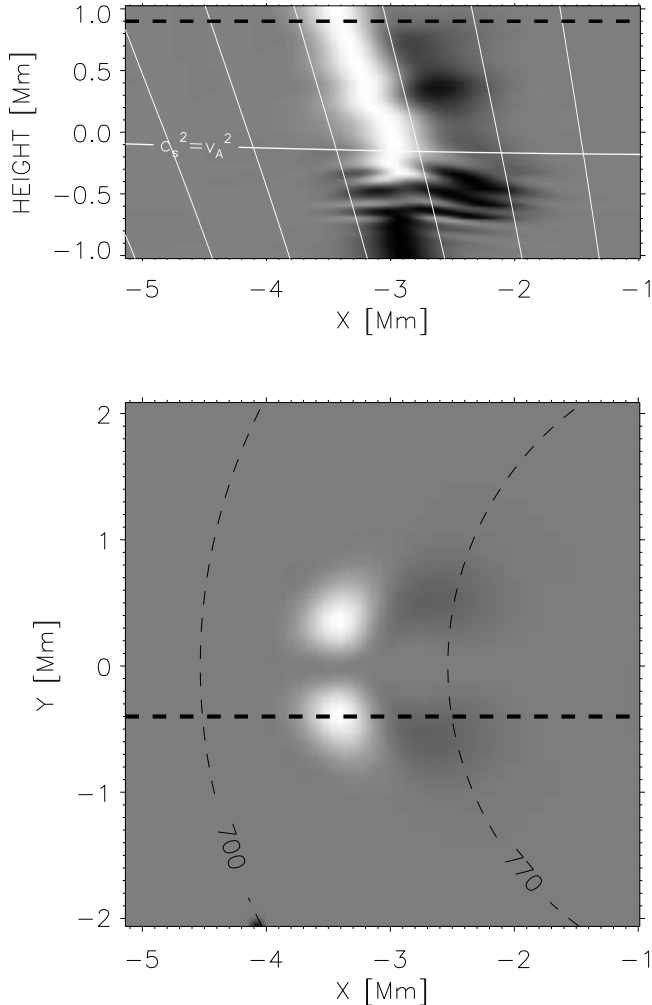


FIG. 11.— Magnetic flux of the Alfvén mode. *Top*: Vertical cut in the plane $y = -0.4$ Mm, normalized at every height. Vertical white lines are magnetic field lines and horizontal white line is the layer where $c_S^2 = v_A^2$. *Bottom*: Horizontal cut in the plane $z = 0.9$ Mm. Thin dashed lines are contours of equal magnetic field. In both panels, thick dashed lines mark the location of the other plot.

Figure 13 shows vertical snapshots of several variables after 820 s of the simulation with the driver emitting a spectrum of waves with a central frequency at 3.33 mHz given by the Eq. (29).

According to the stratification of the atmosphere, at the axis of the sunspot at $z = -700$ km the cut-off frequency is $\nu_c = 3.3$ mHz. It increases with height reaching a maximum at the height of $z = 0$ km, where its value is $\nu_c = 5.8$ mHz. It means that 5 minute acoustic waves can not propagate upwards above $z = 0$ Mm, since they are evanescent in the vertical direction, and can only propagate horizontally. Therefore, the cut-off frequency is a critical value for the wave propagation in this case, and the behavior of waves below and above the cut-off layer is expected to be completely different.

The source located at $z = -500$ km drives waves with frequencies below as well as above ν_c , but most of its energy goes to the band around 3.33 mHz. This generates a fast acoustic wave with an amplitude below 100 m s $^{-1}$ and 5 minute period, which can propagate upwards only

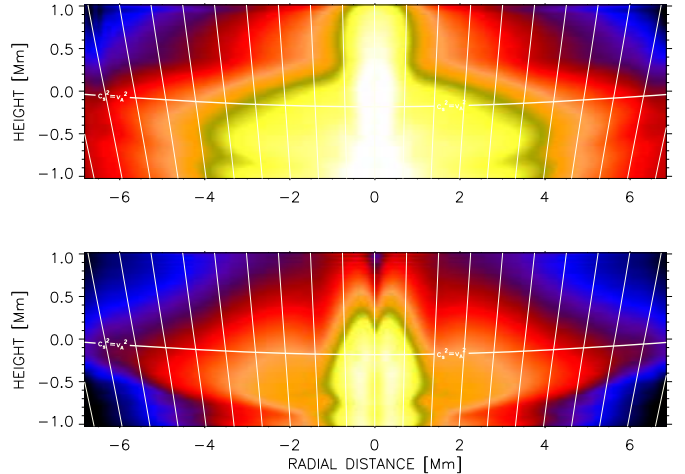


FIG. 12.— Acoustic (*top*) and magnetic (*bottom*) flux for the simulation with a 3 min harmonic driver located at the axis of the sunspot averaged over the stationary stage of the simulations. The format is the same as Fig. 4.

until the height $z = 0$ Mm. Waves with this frequency are evanescent at higher layers and their vertical wavelength occupies the whole upper part of the simulated atmosphere. The amplitude of their longitudinal velocity slightly increases with height.

3.7.1. Three-dimensional mode transformation

Part of the energy of the driver which reaches the surface $v_A^2 = c_S^2$ is transformed into a fast wave above this height. Due to its magnetic nature it becomes unaffected by the cut-off frequency. As in the previous simulations, the transversal velocity in Fig. 13b and the transversal magnetic field in Fig. 13d show that the fast magnetic wave in the region $v_A > c_S$ is reflected because of the gradients in the Alfvén speed. Once the wave comes back to the sub-photospheric layers below $v_A^2 = c_S^2$, it keeps its magnetic nature and propagates downwards in a form of a slow wave with decreasing wavelength due to the drop of the Alfvén speed, but keeping its 5 minute period.

The maximum cut-off frequency at the axis in this sunspot model is $\nu_c = 5.8$ mHz, so waves with higher frequencies can still propagate upwards through the atmosphere. The fast acoustic modes generated by the driver with frequencies higher than ν_c are transformed into propagating slow acoustic modes in the region above $v_A^2 = c_S^2$. The contours in Fig. 13a represent constant longitudinal velocity. At a height around $z = 900$ km, the longitudinal velocity has maximum power at 3 minute period, which corresponds to the frequency above ν_c receiving more energy from the driver.

3.7.2. Frequency change with height

The increase of the amplitude of 3-minute waves according to the drop of the density (compared to much weaker increase of the amplitude of the evanescent 5-minute waves) leads to the power spectrum at chromospheric heights dominated by 3-minute waves. There, their amplitudes reach almost 400 m s $^{-1}$. They do not develop into a saw-tooth waves because at the photosphere the driver generates low power at this frequency band and their amplitude increase is not enough to produce significant non-linearities.

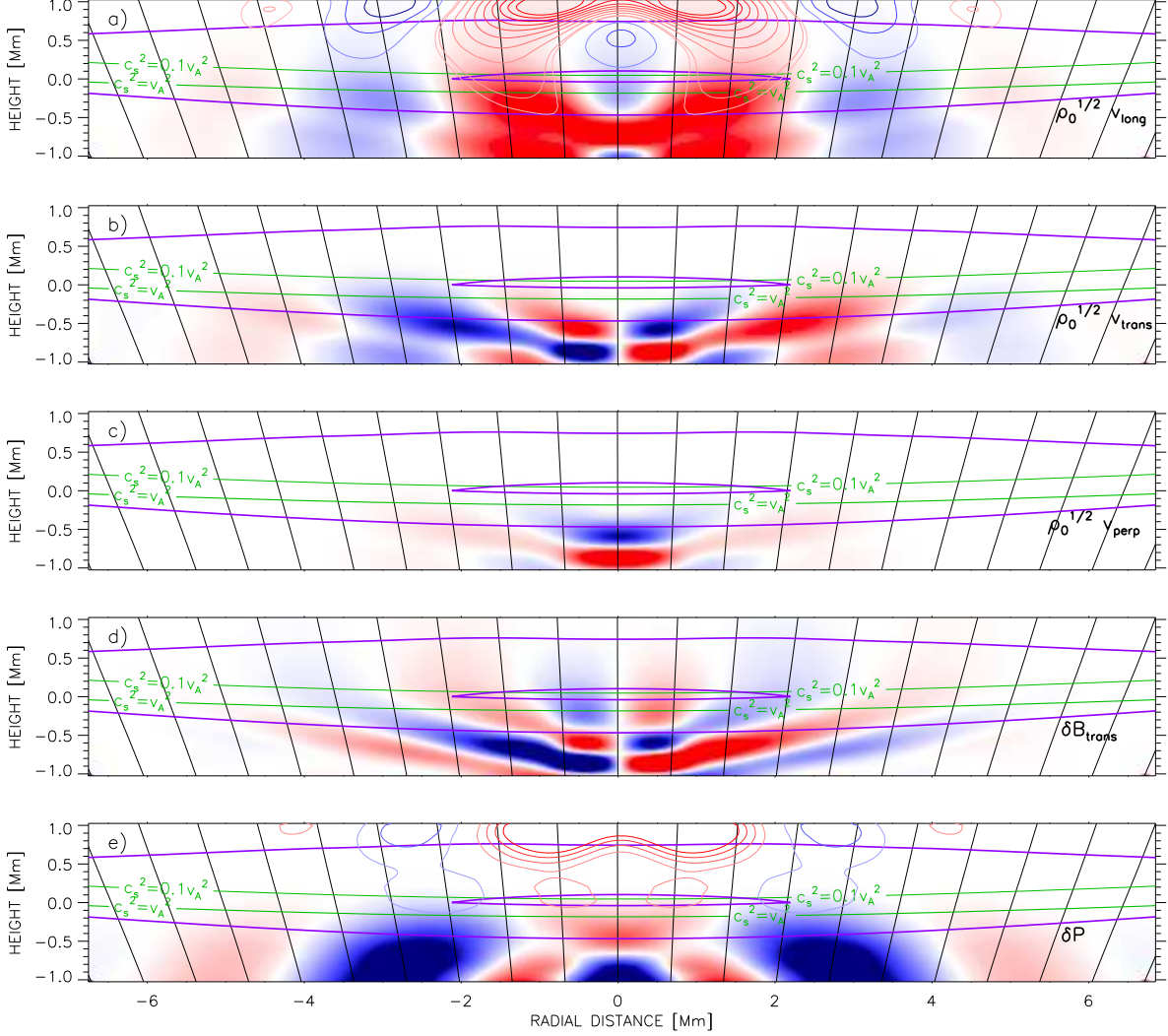


FIG. 13.— Variations of the velocity in the direction \hat{e}_{long} (a), \hat{e}_{trans} (b), and \hat{e}_{perp} (c), all of them scaled with factor $\sqrt{\rho_0}$ of the unperturbed density; magnetic field in the direction \hat{e}_{trans} (d), and pressure (e) at an elapsed time $t=820$ s after the beginning of the simulations for the 300 s wavelet force located at $x = 0$ km, $y = 0$ km and $z = -500$ km. The format of the figure is the same as Fig. 1. Violet lines represent contours of equal cut-off frequency. The inner one is $\nu_c = 5.6$ mHz and the outer one is $\nu_c = 4$ mHz.

Figure 14 shows the power spectra at different heights, from $z = -250$ to $z = 750$ km. At $z = 750$ km it shows a clear peak at $\nu = 5.9$ mHz, corresponding to a period of 170 s. At the lower layers, a peak below 4 mHz dominates. One can see in this figure how the amplitude of the low-frequency peak increases with height. However, this increase is weaker than the one of the peak at high-frequency around $\nu \approx 6$ mHz. Due to this behaviour, the high layers are dominated by oscillations with period around 3 minutes.

A simulation with a 300 s harmonic driver was also performed. In this case high layers develop evanescent 5 minutes period waves, but there is no trace of 3 minutes oscillations at the chromosphere, so power in this frequency band can not be produced if these frequencies are not excited by the driver. Thus, we can conclude that the mechanism that produces the change in frequency of oscillations in the umbra from the photosphere to the chromosphere is the linear propagation of waves with 3 minute power which come directly from the photosphere and dominate over the evanescent long period

waves. This conclusion goes in line with the results of the observational study of sunspot waves simultaneously at the photosphere and the chromosphere by Centeno et al. (2006).

3.7.3. Acoustic and magnetic wave energy fluxes

The magnitudes $\sqrt{\rho_0}v_{\text{long}}$, $\sqrt{\rho_0}v_{\text{tran}}$ and $\sqrt{\rho_0}v_{\text{perp}}$ plotted in Fig. 13 (panels a–c), respectively, show that most of the kinetic energy remains in the photosphere and below. Most of the energy introduced by the driver goes into the waves in the 5 minute band. Propagating to higher layers, they form evanescent waves or are transformed into fast magnetic mode waves. The first ones do not carry energy, while the second ones are reflected back to the photosphere. Thus, waves in the 5 minute band can not supply energy to the chromosphere, if the driving force is located at the sunspot center.

This case differs from the simulations with shorter periods described in Sects. 3.4, 3.5 and 3.6, where the slow acoustic wave transports to the high layers part of the energy injected by the driver (or, in the case of 50 s off-axis

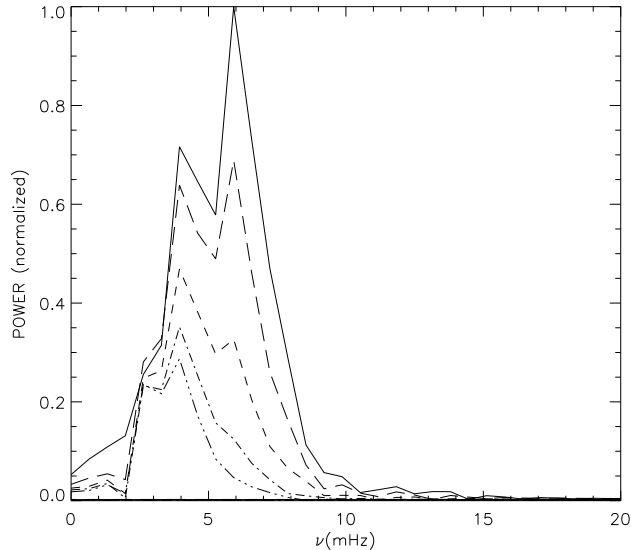


FIG. 14.— Power spectra at different heights at the axis of the sunspot for the simulations with 300 s wavelet force, normalized to the maximum power at the highest height. From bottom to top: $z = -250$ km, $z = 0$ km, $z = 250$ km, $z = 500$ km and $z = 750$ km.

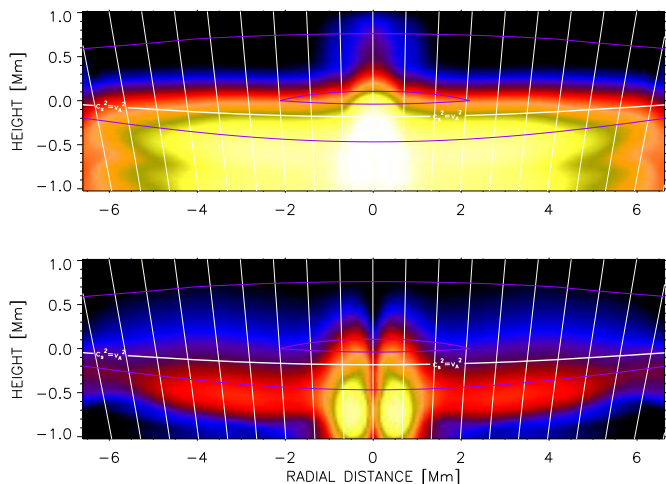


FIG. 15.— Acoustic (*top*) and magnetic (*bottom*) flux for the simulation with a 5 min wavelet driver located at the axis of the sunspot averaged over the stationary stage of the simulations. The format is the same as Fig. 4. Violet lines represent contours of equal cut-off frequency. The inner one is $\nu_c = 5.6$ mHz and the outer one is $\nu_c = 4$ mHz.

driver, a smaller part of the energy is also transported upwards in the form of the Alfvén wave). In the simulation with the 5 minute wavelet force located at the axis, only the waves with frequencies higher than ν_c can provide energy to the chromosphere, and they represent a small fraction of the energy introduced by the driver.

The acoustic flux in Fig. 15 shows that most of the energy keeps below the layer $c_S^2 = v_A^2$. The wavelet mainly drives 5 min power in a fast acoustic mode, and since it is evanescent, it does not propagate energy upwards and this 5 min power is distributed horizontally. Only waves with frequency higher than the cut-off frequency are transformed into slow acoustic modes in the low- β region and carry energy to the chromosphere. They correspond to the low acoustic flux which appears at the

center of the sunspot between $z = 0$ Mm and $z = 1$ Mm. The high- β region contains the energy of the slow magnetic modes generated from the secondary transformation of the reflected fast magnetic modes. In the magnetic flux, the energy of these slow modes appears in red for radial distances below 6 Mm. Note that, interestingly, the maximum of this energy is not located just at the $c_S^2 = v_A^2$ line it was in the case of 50 s simulations, but it located below this line. This new location follows the line of constant $\nu_c = 4$ mHz meaning that the cut-off effects influence also the penetration of the magnetic energy into the higher layers. The fast mode waves in the high- β region contribute to the high acoustic flux there. Like in all the simulations with the driver located at the center of the sunspot, magnetic flux along field lines is negligible, and there is no conversion to Alfvén waves.

3.7.4. Propagation in the upper atmosphere

Contours in Fig. 13a in the region above $v_A^2 = c_S^2$ (upper part of the domain) far from the axis of the sunspot show longitudinal waves with 5 minute period which apparently move across field lines at the sound speed. Similar to Sect. 3.4, we tried to analyze their wave number and phase velocity behavior with height. However, the wavelength of these waves in the upper layers is comparable to the size of our simulation domain in the vertical direction (~ 1 Mm above $v_A^2 = c_S^2$). Because of that, we can not be completely sure if these waves propagate along or across the field lines.

Another difficulty to understand the behavior of these waves lies in the fact that their frequency is below the cut-off frequency ν_c of the atmosphere. In principle, the cut-off frequency in the magnetically dominated atmosphere is lowered for the acoustic wave propagating along inclined field lines. We calculated the cut-off frequency taking into account the effect of the field inclination. We found this inclination to be insufficient to reduce the cut-off frequency enough to allow for the propagation of the 5-minute waves. Simulations in a larger spatial domain (both in the horizontal and vertical direction) will be needed in the future to clarify the nature of these waves.

4. CONCLUSIONS

In this paper, we have addressed the problem of the three-dimensional wave propagation and mode transformation of the MHD waves in the upper atmosphere (photosphere and chromosphere) of a sunspot model, by means of numerical simulations. We have presented our code for the calculation of the response of a magnetostatic structure in equilibrium to an arbitrary perturbation. This code is specially designed to model the wave propagation in solar magnetic structures with non-trivial magnetic field configurations. We performed several tests proving the correct code performance. The comparison of the numerical tests with the analytical solutions (when they are available) or with the results from other codes (in other cases) shows a precise agreement and demonstrates the robustness of the numerical method applied in this code according to several aspects: the velocities of wave propagation, the resolution of shocks and the conservation of energy. The performance of the artificial diffusivity makes it possible to resolve strong discontinuities with a few grid points and without producing damping of the solution, and the energy is well conserved. The PML

boundary condition allows us to calculate long temporal series of simulations without reflections of the waves reaching the top boundary.

We have presented the analysis of several simulations where the sunspot atmosphere was perturbed by different pulses, varying their location and temporal behaviour. The simulations of short period waves in the three-dimensional sunspot model clearly show several phenomena that are predicted by wave theory. We confirmed that our code correctly describes the propagation of slow and fast modes, both in regions dominated by the magnetic field or the gas pressure. Our main findings, learned from the simulations, can be summarized as follows:

- The conversion between fast and slow magneto-acoustic waves happens in three dimensions in a qualitatively similar way as in two dimensions. Waves with frequencies down to the cut-off frequency behave in the same way. The driver located in the gas pressure dominated region generates mostly the fast (acoustic) mode. This mode, propagating to the upper layers, is transformed at the height where $c_S = v_A$. After the transformation, a slow acoustic mode propagates upwards along the field lines in the magnetically dominated atmosphere. The fast magnetic mode undergoes refraction and it is reflected back to the sub-photosphere. When it reaches again the surface $c_S = v_A$, new transformations take place producing another fast acoustic and slow magnetic modes in the region $v_A < c_S$.
- High-frequency field-aligned propagating acoustic waves are constantly produced in the upper magnetically dominated atmosphere at locations away from the source. These waves appear due to the continuous transformation from the fast (acoustic) waves moving horizontally, across the field lines, away from the source in the gas pressure dominated region. On their way, the fast waves constantly touch the $c_S = v_A$ layer producing slow (acoustic) waves in the upper atmosphere in the horizontal locations far from the source. We observe this behaviour in all simulations with different driving frequencies and source position.
- The 3D simulations allow us to identify an Alfvén mode. This mode appears only in the simulation with the source located away from the sunspot axis. It is produced after the transformation from the fast (acoustic) mode. We find that the transformation efficiency from the fast to the Alfvén mode is much lower than that from the fast to the slow mode. The eventual energy of the Alfvén wave in the magnetically dominated region is 20 times lower than that of the slow mode. In the simulations with the driver located at the axis of the sunspot, where the angle between the direction of the upwards propagating wave and the magnetic field is zero, we find no indications of the transformation to the Alfvén mode.
- The analysis of the wave energy fluxes suggests that in the high-frequency cases (above the cut-off)

the wave energy can reach the upper atmosphere most efficiently in the form of slow (acoustic) field aligned propagating waves. After some height in the middle photosphere there is no magnetic flux corresponding to the fast (magnetic) waves as their energy is reflected. If the driver is located away from the axis, some small part of the energy also can propagate upwards in the form of an Alfvén wave.

- Both magnetic and acoustic energy of the low-frequency waves (smaller than the cut-off) remain almost completely below the level $c_S = v_A$ and do not reach upper layers. This happens because the energy of the fast magnetic modes in the upper layers is reflected, and the evanescent acoustic slow modes do not propagate any energy at these frequencies. The comparison between the magnetic fluxes at high and low frequencies shows that the magnetic flux reaches smaller heights for the low-frequency waves.
- When the driver excites a spectrum of waves, we observe a change of the dominant frequency of oscillations with height from the photosphere to the chromosphere. The driver excites a spectrum with a maximum power at 3.33 mHz frequency. Waves at this frequency are evanescent in the atmosphere. At higher frequencies (above $\nu_c = 5.8$ mHz in our sunspot model) the waves can propagate upwards along the field lines. Due to the larger amplitude increase with height of the propagating waves, compared to the evanescent waves, the 3-minute waves ($\nu \approx 5.9$ mHz) dominate the power spectrum in the chromosphere. This behavior, obtained in the simulations, is similar to the observed one.

One of the questions that arises from these results is the evaluation of the validity of the decomposition performed to separate the fast mode from the Alfvén mode in the low-beta plasma. The decoupling following Cally & Goossens (2008) is valid for an idealized case when considering a uniform magnetic field, for a plane wave with a constant wavenumber perpendicular to gravity, and it is obtained asymptotically in the limit of infinite Alfvén speed. Although the realistic atmosphere used in our calculations does not fulfill these restrictions, a coherent picture is retrieved from the magnetic flux of the velocity and magnetic field components in the direction given by Eq. 34, showing upwards propagation along magnetic field lines. The result that naturally emerges from this decomposition justifies the application of the method.

Another issue that complicates the decoupling of both modes is the excitation of small horizontal wavenumbers due to the limited horizontal extent of the driver. The fast mode is refracted due to the rapid increase of the Alfvén speed with height, but the altitude at which it happens depends on the wavenumber, being higher for lower wavenumbers. Since most of the power excited by our driver lies in the range of wavenumbers below $\sim 1/R_{scr}$, some of the fast mode waves might still be partially refracted in the limited 1 Mm atmosphere above the $c_S = v_A$ surface. The magnetic flux of these waves may reach high layers, complicating the separation of

the fast and Alfvén modes. In this scenario, we would expect a continuous transition between the upward longitudinal magnetic flux and the refracted one at different heights where all these waves are being refracted. However, the magnetic flux of the Alfvén wave that we retrieve is clearly delimited along magnetic field lines, confirming that this flux mostly corresponds to the Alfvén mode.

The most important achievement reached by the development of our numerical code is the possibility to investigate the three-dimensional mode transformation in realistic conditions imitating a sunspot atmosphere. This, together with the possibility to study large-period waves in the layers where they are observed, gives an opportunity for the direct comparison between our numerical simulations and solar spectropolarimetric observations. Simulations of sunspot high layers represent a hard challenge due to the exponential increase of the Alfvén speed with height. Our sunspot model presents an Alfvén speed of almost 1000 km s^{-1} close to the upper boundary of the domain, limiting the time step and making the calculations very expensive. Despite this, our code manages to describe the waves well, including the correct performance of the boundary PML layer. Note that other works on waves in non-trivial magnetic configurations have been restricted either to two-dimensional high-frequency cases (Cargill et al. 1997; Rosenthal et al. 2002; Hasan et al. 2003; Bogdan et al. 2003; Khomenko & Collados 2006) or to the study of helioseismic waves, where the problem of high Alfvén speed is avoided (Cally & Bogdan 1997; Parchevsky & Kosovichev 2009; Hanasoge 2008; Cameron et al. 2008; Moradi et al. 2009b; Khomenko et al. 2009).

The strategy applied in our code allows the direct comparison with observations by means of spectral synthesis. The simulations presented in the paper reproduce the frequency change with height, indeed observed in the sunspot atmospheres (Centeno et al. 2006). In the future we plan to perform a more detailed comparison with solar data. This will be done by exciting the sunspot magnetostatic model in equilibrium with velocities obtained from

spectropolarimetric observations, and by comparison of the simulated wave parameters in the photosphere and chromosphere with those obtained from simultaneous observations in different spectral lines.

Perhaps the most interesting simulation considered in our paper is the one with the source exciting a spectrum of waves close to the solar one. This case has a special relevance because theoretical models of wave transformation, existing as of today, are best valid in the high-frequency limit and do not address the behavior of waves at frequencies below the cut-off frequency (Schunker & Cally 2006). Our initial results show that almost no energy of the 5-minute waves propagates into the higher layers, at least in the situation of the sunspot model and source located at the axis considered in the paper. These results need further exploration. In our future work we will perform simulations of 5-minute waves in larger computational boxes, varying the excitation mechanisms (location and properties of the source), as well as the sunspot model. In particular, an interesting question is under which conditions 5-minute Alfvén waves can be excited by the mode transformation. These waves can still propagate some energy into the upper atmosphere of solar active regions, and thus understanding the conditions of transformation to these waves and their energetics in sunspots is important. The number of works in the literature with numerical calculations including the transformation to Alfvén waves is scarce. The most relevant study is the one by Cally & Goossens (2008) who find that the transformation to an Alfvén mode is effective at certain angles of inclination and azimuth of the magnetic field.

This research has been funded by the Spanish MICINN through projects AYA2007-63881 and AYA2007-66502. The simulations have been done on LaPalma supercomputer at Centro de Astrofísica de La Palma and on MareNostrum supercomputer at Barcelona Supercomputing Center (the nodes of Spanish National Supercomputing Center). To represent the data we have used VAPOR software (<http://www.vapor.ucar.edu>).

REFERENCES

- Avrett, E. H. 1981, in *The physics of sunspots*, Vol. 257, Sunspot, NM, Sacramento Peak Observatory, 235–255
- Balsara, D. S., & Spicer, D. S. 1999, *J. Comp. Phys.*, 149, 270
- Beckers, J. M., & Tallant, P. E. 1969, *Solar Phys.*, 7, 351
- Berenger, J. P. 1994, *J. Comp. Phys.*, 114, 185
- , 1996, *J. Comp. Phys.*, 127, 363
- Bloomfield, D. S., Lagg, A., & Solanki, S. K. 2007, in *The Physics of Chromospheric Plasmas*, ed. P. Heinzel, I. Dorotovic, & R. J. Rutten, Vol. 368, ASP Conference Series, 239
- Bogdan, T. J., Carlsson, M., Hansteen, V., et al. 2003, *ApJ*, 599, 626
- Bogdan, T. J., & Judge, P. G. 2006, in *MHD wave and oscillations in the Solar Plasma*, Vol. 364, Issue 1839 (Phil. Trans. Royal. Soc.), 313–331
- Bray, R. J., & Loughhead, R. E. 1974, *The Solar Chromosphere*, Chapman and Hall, London, 252
- Brio, M., & Wu, C. 1988, *J. Comp. Phys.*, 75, 400
- Cally, P. 2005, *MNRAS*, 358, 353
- , 2006, *Phil. Trans. R. Soc. A*, 364, 333
- Cally, P. S. 1995, *ApJ*, 451, 372
- Cally, P. S., & Bogdan, T. J. 1997, *ApJ*, 486, L67
- Cally, P. S., & Goossens, M. 2008, *Sol. Phys.*, 251, 251
- Cameron, R., Gizon, L., & Daifallah, K. 2007, *Astronomische Nachrichten*, 328, 313
- Cameron, R., Gizon, L., & Duvall, Jr., T. L. 2008, *Sol. Phys.*, 251, 291
- Cargill, P. J., Spicer, D. S., & Zalesak, T. 1997, *ApJ*, 488, 854
- Caunt, S. E., & Korpi, M. J. 2001, *A&A*, 369, 706
- Centeno, R., Collados, M., & Trujillo Bueno, J. 2006, *ApJ*, 640, 1153
- Christensen-Dalsgaard, J., Dappen, W., Ajukov, S. V., & 30 co-authors. 1996, *Science*, 272, 1286
- Dai, W., & Woodward, P. R. 1998, *ApJ*, 494, 317
- Ferraro, V. C. A., & Plumpton, C. 1958, *ApJ*, 127, 459
- Goldreich, P., & Keeley, D. A. 1977, *ApJ*, 211, 934
- Goldreich, P., & Kumar, P. 1988, *ApJ*, 326, 462
- , 1990, *ApJ*, 363, 694
- Gurman, J. B., & Leibacher, J. W. 1984, *ApJ*, 283, 859
- Hanasoge, S. M. 2008, *ApJ*, 680, 1457
- Hasan, S. S., Kalkofen, W., van Ballegoijen, A. A., & Ulmschneider, P. 2003, *ApJ*, 585, 1138
- Hasan, S. S., van Ballegoijen, A. A., Kalkofen, W., & Steiner, O. 2005, *ApJ*, 631, 1270
- Hasan, S. S., & Ulmschneider, P. 2004, *A&A*, 422, 1085
- Hesthaven, J. S. 1998, *J. Comp. Phys.*, 142, 129

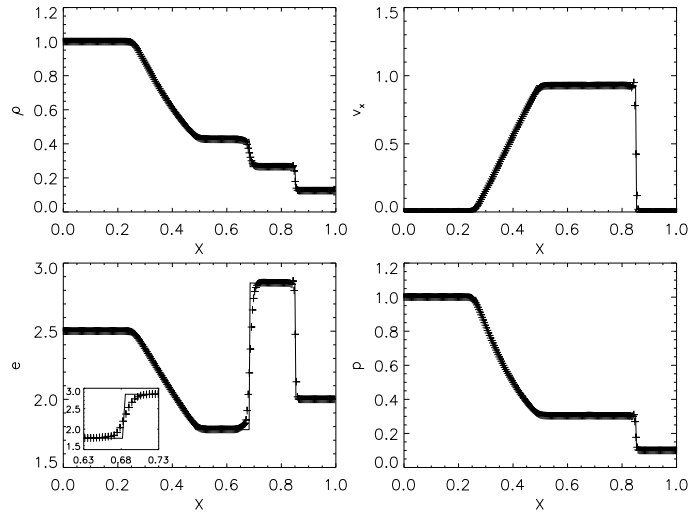


FIG. 16.— Standard Riemann shock tube problem at $t = 0.2$. Crosses represent numerical solution, while lines represent the analytic solution with an exact nonlinear Riemann solver. Inner plot on left bottom panel helps to visualize better the discontinuity at $x = 0.68$.

Hindman, B. W., Jain, R., & Zweibel, E. G. 1997, *ApJ*, 476, 392
 Hu, F. Q. 1996, *J. Comp. Phys.*, 129, 201
 —. 2001, *J. Comp. Phys.*, 173, 455
 Khomenko, E. 2010, *ASPCs*, 416
 Khomenko, E., & Collados, M. 2006, *ApJ*, 653, 739
 Khomenko, E., & Collados, M. 2008, *ApJ*, 689, 1379
 Khomenko, E., Collados, M., & Felipe, T. 2008, *Sol. Phys.*, 251, 589
 Khomenko, E., Kosovichev, A., Collados, M., Parchevsky, K., & Olshevsky, V. 2009, *ApJ*, 694, 411
 Khomenko, E. V., Collados, M., & Bellot Rubio, L. R. 2003, *ApJ*, 588, 606
 Leighton, R. B., Noyes, R. W., & Simon, G. W. 1962, *ApJ*, 135, 474
 Lites, B. W. 1986, *ApJ*, 301, 1005
 Londrillo, P., & Del Zanna, L. 2000, *ApJ*, 530, 508
 Mihalas, D., & Mihalas, B. W. 1984, *Foundations of Radiation Hydrodynamics* (Oxford: Oxford University Press)
 Moradi, H., Baldner, C., Birch, A. C., et al. 2009a, *ArXiv e-prints*
 Moradi, H., Hanasoge, S. M., & Cally, P. S. 2009b, *ApJ*, 690, L72
 Orszag, M., & Tang, C. 1979, *J. Fluid Mech.*, 90, 129
 Parchevsky, K. V., & Kosovichev, A. G. 2007, *ApJ*, 666, L53
 Parchevsky, K. V., & Kosovichev, A. G. 2009, *ApJ*, 694, 573

Rosenthal, C. S., Bogdan, T. J., Carlsson, M., et al. 2002, *ApJ*, 564, 508
 Ryu, D., Jones, T. W., & Frank, A. 1995, *ApJ*, 452, 791
 Schunker, H., & Cally, P. S. 2006, *MNRAS*, 372, 551
 Shelyag, S., Fedun, V., & Erdélyi, R. 2008, *A&A*, 486, 655
 Shelyag, S., Zharkov, S., Fedun, V., Erdélyi, R. & Thompson, M. J. 2009, *A&A*, 501, 735
 Zharkov, S.; Fedun, V.; Erdlyi, R.; Thompson, M. J.
 Sod, G. A. 1978, *J. Comp. Phys.*, 27, 1
 Stein, R. F., & Nordlund, Å. 1998, *ApJ*, 499, 914
 Stone, J., & Norman, M. 1992, *ApJS*, 80, 791
 Tóth, G. 1996, *Astrophysical Letters Communications*, 34, 245
 van der Voort, L. H. M. R., Rutten, R. J., Sütterlin, P., Sloover, P. J., & Krijger, J. M. 2003, *A&A*, 403, 277
 Vernazza, J. E., Avrett, E. H., & Loeser, R. 1981, *ApJ*, 45, 635
 Vögler, A., Shelyag, S., Schüssler, M., Cattaneo, F., Emonet, T., & Linde, T. 2005, *A&A*, 429, 335
 Woods, D. T., & Cram, L. E. 1981, *Sol. Phys.*, 69, 233
 Zhugzhda, I. D., Locans, V., & Staude, J. 1985, *A&A*, 143, 201
 Zhugzhda, Y. D., & Dzhililov, N. S. 1984, *A&A*, 132, 45

APPENDIX

TESTS ON NUMERICAL PERFORMANCE

In this appendix we describe the results of standard numerical tests to verify the code performance.

1D Riemann shock tube test

The Riemann shock tube test (Sod 1978; Caunt & Korpi 2001) has been simulated in order to test the behavior of the hydrodynamical part of the code, including discontinuities in the properties of the fluid. This allow us to analyze how the artificial viscosity copes with shock capturing. The physical domain size is unity and the initial conditions include a discontinuity at $x = 0.5$. On the left we have density $\rho_1 = 1$ and pressure $p_1 = 1$, while on the right $\rho_1 = 0.125$ and $p_1 = 0.1$. The ratio of specific heats is $\gamma = 1.4$ and the initial velocity as well as the magnetic field are set to zero. The problem has been simulated in one dimension with a resolution of 256 grid points and closed boundaries.

Figure 16 shows the density, velocity, internal energy density per unit mass and pressure at time $t=0.2$ for the simulation compared to the analytical solution. From left to right the plot shows a rarefaction wave (from $x = 0.25$ to $x = 0.5$), a contact discontinuity (at $x = 0.68$) and a shock front ($x = 0.85$). The position of all of them matches precisely with the analytical solution and the magnitudes of the fluid properties are correct. The contact discontinuity for the energy was inevitably smoothed, as shown in the plot at the bottom left where a region around it is amplified, but still a 93% of the amplitude of the discontinuity is covered with 10 grid points. Moreover, the shock front is resolved with 3 grid points, which proves the good performance of the code in shock capturing.

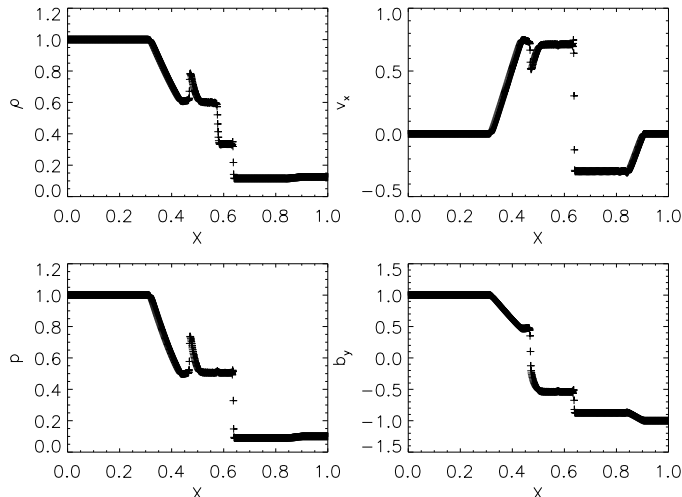


FIG. 17.— Numerical solution of the Brio & Wu problem at $t=0.11$ (see § A.2).

1.5D Brio & Wu shock tube

To test the formation of magnetohydrodynamic shock waves we use the MHD analog of the Sod shock tube problem described by Brio & Wu (1988), which has been widely used in previous works (Stone & Norman 1992; Caunt & Korpi 2001; Shelyag et al. 2008). We can compare our results with those given in the literature, since no known analytical solution exists for the evolution of this problem. In this 2D test the fluid is initialized in a physical domain from $x = 0$ to $x = 1$ and with a discontinuity in density, pressure and magnetic field normal to the direction of motion located at $x = 0.5$. Parameters at the left hand side from the discontinuity are $\rho_1 = 1$, $p_1 = 1$ and $B_{y1} = \sqrt{\mu_0}$, and at the right hand side are $\rho_2 = 0.1$, $p_2 = 0.1$ and $B_{y2} = -\sqrt{\mu_0}$. All the domain is permeated with a constant magnetic field along the direction of motion $B_x = 0.75\sqrt{\mu_0}$ and the adiabatic index γ is set to 2. In this case the resolution is 800 grid points in the direction of the shock wave propagation, similar to the other published works. All the boundaries are closed.

The density, velocity in x direction, pressure and magnetic field in y direction are shown in Figure 17. This MHD Riemann problem produces a complex solution with several components: the waves moving to the left are a fast rarefaction wave and a slow compound wave (consisting of a slow rarefaction attached to a slow shock), and the waves moving to the right include a contact discontinuity, a slow shock and a fast rarefaction wave. Comparison of our results with other works show that the waves have propagated with the correct velocities and have similar magnitudes, indicating that they are in good agreement with other solutions. The slow shock is resolved again with only 3 grid points.

2D Ország-Tang vortex

The next test is the Orszag-Tang vortex, which was originally studied by Orszag & Tang (1979) and has been used to probe several codes (Ryu et al. 1995; Dai & Woodward 1998; Londrillo & Del Zanna 2000; Shelyag et al. 2008). This problem allows us to demonstrate the robustness of the numerical scheme used in our code solving the two-dimensional interaction of non-linear shock-waves and also to compare qualitatively the code with other codes. The initial conditions for density and gas pressure are constant, with $\rho = 25/(36\pi)$ and $p = 5/(12\pi)$, the magnetic field $B_x = -\sin(2\pi y)$ and $B_y = \sin(4\pi x)$ and the initial velocity $v_x = -\sin(2\pi y)$ and $v_y = \sin(2\pi x)$. Therefore, the initial flow is a velocity vortex superimposed to a magnetic vortex, with a common X-point, but with different structure. The initial Mach number is $M_0 = 1$ and the adiabatic index is set to $\gamma = 5/3$. In our simulation for this problem we have chosen a unit size in horizontal and vertical dimensions and the resolution of the simulation box is set to 512×512 grid points. Figure 18 presents the density at time $t = 0.5$, showing precise agreement with the other published works.

3D Acoustic wave

Since our code is oriented for the simulations of waves, it is necessary to test how well it can approximate the known analytical solutions for different types of waves in a stratified atmosphere, their propagation speeds, amplitudes and shock development. The analytical solution of an acoustic wave propagating in an isothermal atmosphere with vertical stratification due to gravity and permeated with a constant vertical magnetic field is known from Ferraro & Plumpton (1958). The vertical velocity for wave with frequencies ω above the cut-off frequency $\omega_c = \gamma g/(2c_S)$ follows as:

$$v_z(z, t) = D e^{z/2H_0} \sin \left[\left(\frac{\sqrt{\omega^2 - \omega_c^2}}{c_S} z + \omega t \right) \right], \quad (\text{A1})$$

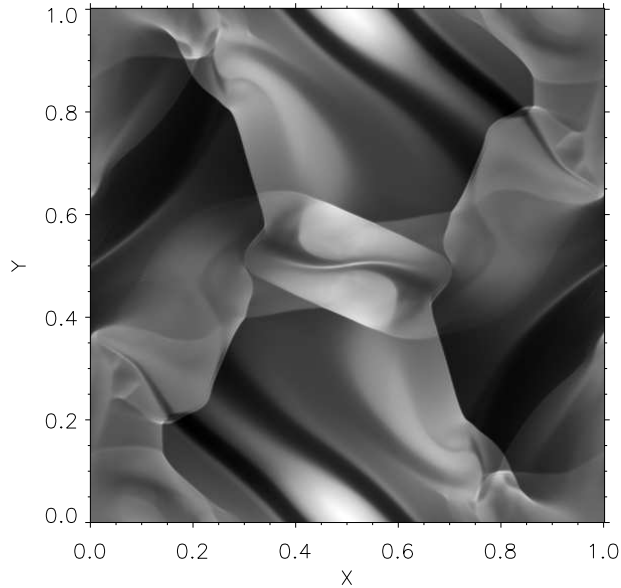


FIG. 18.— Mass density at $t=0.5$ of the Ország-Tang vortex simulation.

where $H_0 = c_S^2/(\gamma g)$ is the pressure scale height and c_S is the sound speed. This analytical solution with a period of 15 s and starting amplitude of 10 m s^{-1} has been introduced as a bottom boundary condition without variations in the horizontal directions and its evolution in time has been calculated with the numerical code. The physical domain is set to 1000 km in the vertical direction with a resolution of 200 grid points, using 20 of them as PML domain at the top. In both horizontal dimensions the computational domain consists of 7 grid points, covering 35 km, and periodic boundary conditions were used in these directions. In Fig. 19 we show the comparison between the numerical and the analytical linear solution for the vertical velocity after 197 s of simulations. The numerical solution matches the exact solution in the computational domain, while it is damped effectively by the PML layer. It is important to note that the amplitude and propagation speeds are both described correctly by the numerical solution and that the numerical diffusion does not affect the amplitude increase with height. No spurious reflections are present showing the correct action of the PML boundary in this example.

The dashed line represents the difference between both solutions, which also increases with height. The main contribution to this difference are the nonlinear terms that are taken into account in the numerical calculation, but not in the analytical solution. We have checked that reducing the driver amplitude by a factor of two reduces the difference by exactly a factor of four. The wavelength of the difference is twice shorter compared to that of the wave. These two arguments prove that the difference between the analytical and numerical solutions is mostly due to non-linear terms.

3D Alfvén wave

As a next step, the response of the numerical scheme to the propagation of an Alfvén wave in an isothermal, stratified atmosphere with vertical magnetic field is analyzed. The analytical solution was developed by Ferraro & Plumpton (1958), and, according to Khomenko et al. (2003), the solution for the horizontal velocity can be written as

$$v_y(z, t) = i\xi_0\omega\sqrt{J_0^2 + Y_0^2}\exp\left[i\left(\omega t + \arctan\frac{Y_0}{J_0}\right)\right] \quad (\text{A2})$$

where J_0 and Y_0 are Bessel functions and v_A is the Alfvén speed. The same atmosphere as in the previous section was used in this test, but now the bottom layers were excited with the solution of an Alfvén wave of period 10 s and an amplitude of 10 m s^{-1} as a boundary condition. This driver generates the propagation of Alfvén waves toward higher layers of the atmosphere. The horizontal velocity of both the numerical and exact solutions for time $t = 115 \text{ s}$ is shown in Fig. 20, demonstrating a very good match.

The dashed line shows the difference between the numerical and the analytical solution. In this case, the nonlinearities are not so important since the amplitude is lower than the one of the acoustic wave, and the discrepancy between both solutions is due to the reflection produced at the top boundary. The PML layer results more problematic for transversal waves which oscillate parallel to the interface between the PML media and the physical domain, and they give rise to reflections of 5-6% of the velocity.

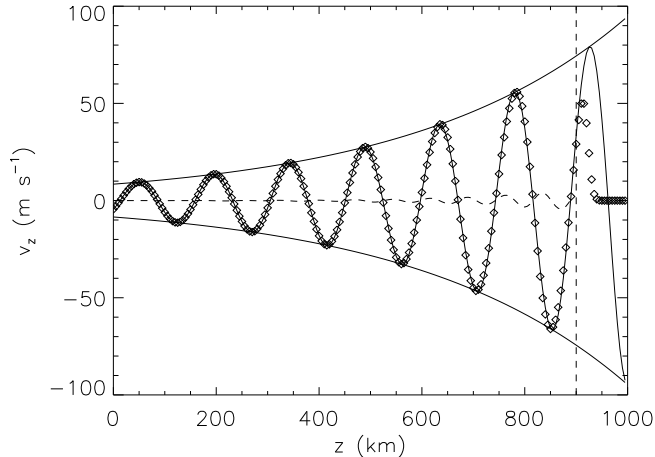


FIG. 19.— Vertical velocity profile of vertically propagating acoustic waves in an isothermal, stratified atmosphere with vertical constant magnetic field at $t=197$ s. Solid line: exact solution; diamonds: numerical solution. Dashed line is the difference between both solutions. The vertical dashed line indicates the location of the PML interface.

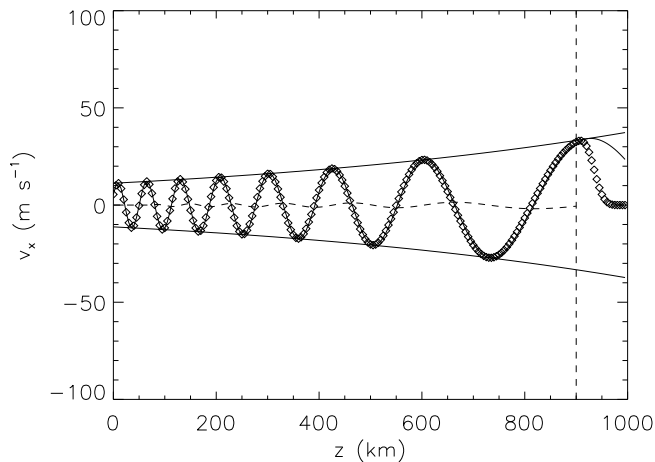


FIG. 20.— Horizontal velocity profile of Alfvén waves in an isothermal, stratified atmosphere with vertical constant magnetic field at $t=115$ s. Solid line: exact solution; diamonds: numerical solution. Dashed line is the difference between both solutions. The vertical dashed line indicates the position of the PML interface.

3D Strong blast wave

Our last test consists of the explosion of a spherical high gas pressure region in a magnetized, initially static 3D medium. It has been commonly used for code validation (see, for example Balsara & Spicer 1999; Londrillo & Del Zanna 2000), and the set-up consists of a cubic domain with 256 grid points in the three spatial dimensions spanning from 0 to 1. The initial density, ρ_0 , is set to unity in all the domain, while the initial pressure is set to unity all over except a spheric hot gas region located at the center of the domain of radius $r_0 = 0.125$, which is a hundred times overpressured ($p_1 = 100$). A constant magnetic field with a strength of $B_0 x = 10\sqrt{\mu_0}$ is initialized along the x -direction.

In Fig. 21 we show a cut of the density in the plane $x - y$ at $z = 0.5$ and $t = 0.02$. The system shows the axial symmetry imposed by the magnetic field. We can identify the different wave modes present in the simulations. The outermost wave corresponds to the fast magnetoacoustic mode, and inside this region there are two wave fronts propagating along the magnetic field, which is a slow magnetoacoustic shock. This test verifies that our code can handle with three dimensional propagation of highly nonlinear waves at the correct propagation speed, resolving the shocks thanks to the hyperdiffusive terms.

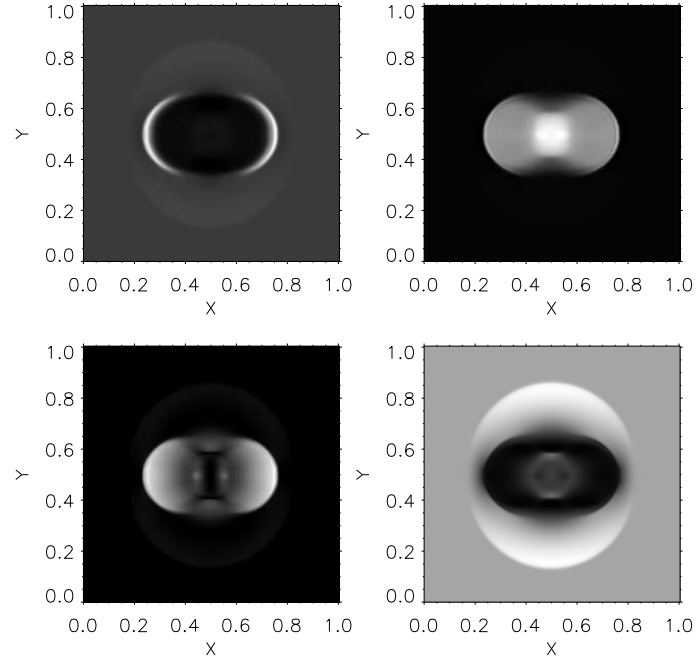


FIG. 21.— Numerical solution of the 3D strong blast wave density at the plane $x - y$ and $z = 0.5$ at $t = 0.02$. From left to right and from top to bottom: Mass density, pressure, velocity squared and magnetic pressure.